https://dx.doi.org/10.1016/j.paerosci.2022.100808

Review of acoustic metasurfaces for hypersonic boundary layer stabilization

Rui Zhao[a], Chihyung Wen[b*], Yu Zhou[c], Guohua Tu[d], Juanmian Lei[a]

[a] *School of Aerospace Engineering, Beijing Institute of Technology, Beijing, 100081, China*
[b] *Department of Aeronautical and Aviation Engineering, The Hong Kong Polytechnic University, Kowloon, Hong Kong, China*
[c] *Beijing Institute of Nearspace Vehicle's Engineering, Beijing, 100076, China*
[d] *State Key Laboratory of Aerodynamics, China Aerodynamics Research & Development Center, Sichuan Mianyang, 621000, China*

Abstract

Hypersonic boundary-layer (BL) transition generates a significant increase in viscous drag and heat flux, which leads to severe restrictions on the performance and thermal protection systems of hypersonic vehicles. Among various passive/active transition control strategies, acoustic metasurfaces demonstrate minimal effects on the mean flow but significantly suppress the Mack second mode. Therefore, it can be considered one of the most promising transition control technologies. Acoustic metasurfaces are planar metamaterial structures that comprise monolayer or multilayer stacks of subwavelength microstructures, which affect unstable modes via acoustic wave manipulations. This paper presents a review of the research progress made on acoustic metasurfaces for hypersonic BL stabilization over the past two decades. Acoustic characteristics and their corresponding stabilization effects on the first and second modes are compared and discussed. Recent improvements in the mathematical modeling of acoustic metasurfaces have been highlighted. An outline of the theoretical, numerical, and experimental investigations is then provided. Finally, a future research potential, especially for broadband design strategies and full direct numerical simulations, is prospected.

Content:

[*]Corresponding author. Tel.: (852) 2766 6644; fax: (852) 3400 2522.

E-mail address: chihyung.wen@polyu.edu.hk (C.Y. Wen)

Nomenclature

A	=	Metasurface admittance
A_r	=	Cavity aspect ratio, $2b/H$
b	=	Cavity half-width
H	=	Pore depth
f_{acs}	=	Normalized acoustic frequency, $f H/a_w$
R	=	Reflection coefficient
r	=	Pore radius
T	=	Temperature
Z	=	Metasurface impedance, $1/A$
t	=	Time
x, y, z	=	Streamwise, normal and spanwise directions
St	=	Stanton number

Greek

ω	=	Angular frequency
ϕ	=	Porosity, $2b/s$
ρ	=	Density
β	=	Absorptive coefficient
δ	=	Boundary-layer thickness

Subscripts

e	=	Parameters at the boundary-layer edge
i	=	Incident waves
r	=	Diffracted waves
w	=	Parameters at the wall
∞	=	Free stream

1. Introduction

1.1. Background

The laminar-to-turbulent boundary layer (BL) transition has been one of the most important frontier problems in fluid mechanics for a long time. From a theoretical perspective, the transition is a transformation from a stable layered flow to a complex chaotic turbulent state; it is a multifold process that evolves in many different routes depending on numerous parameters of mean flow and disturbances [1-8]. On the other hand, the prediction and control of BL transition has wide applications in the aeronautic and aerospace industries. The BL transition generates a significant increase in viscous drag and heat flux, which leads to severe restrictions on the performance and thermal protection systems of hypersonic vehicles. The estimates for the National Aerospace Plane (NASP) indicate that the payload-to-gross-weight ratio would nearly double if the vehicle BL is fully laminar when compared to that for the fully turbulent scenario [9]. Further, early transition causes higher heating, which requires an increased performance of the thermal protection system (TPS), active cooling, or trajectory modification, and this can lead to higher costs and weights of hypersonic vehicles. In addition, an additional peak heat transfer occurs in the transition region, which is slightly

higher than that in the turbulent region [10-12]. Extensive studies have focused on transition mechanisms to control the BL transition and maintain the laminar flow as long as possible [13-15]. It reveals that even for relatively simple two-dimensional (2D) or axisymmetric boundary layers on a flat plate or a sharp cone at zero angle of attack, there are several paths for transition [16]. If freestream disturbances are small, the transition to turbulence along a smooth vehicle surface occurs because of the amplification of the unstable BL mode (path A in [16]) [17]; this path is typical for axisymmetric missiles or cruise vehicles with predominantly 2D leading edges flighting at high altitudes in a low-disturbance environment [8, 18]. Small environmental disturbances enter the BL and excite the first and Mack second modes through the receptivity process. Subsequently, unstable modes develop linearly, and they can be predicted using the stability theory [13]. Finally, unstable modes reach certain amplitudes, and nonlinear and three-dimensional (3D) effects begin to dominate, which leads to the final transition [16]. The first-mode instability is eliminated by natural cooling because the temperature of a hypersonic vehicle surface is relatively low (less than 0.2 of the adiabatic wall temperature); however, the second mode remains unstable and may trigger an early transition [19]. Thus, the study of natural transition suppression of hypersonic vehicles focuses on developing a more effective method to suppress the second mode in the BL.

Kimmel [20] identified the following categories of transition control techniques that can suppress or attenuate the Mack second mode: (1) passives, such as global or local shaping [21, 22], acoustic metasurfaces, such as porous coatings [10], and (2) actives, such as retuned blow-suction [23], CO_2 injection [24,25], and plasma actuators [26]. A comprehensive survey of different types of transition control techniques have been reported in a recent review by Fedorov [27]. Because of the severe heat fluxes and high temperatures around the hypersonic vehicle surface, it renders the active control techniques difficult to be implemented. Therefore, passive techniques are of primary interest. Since the acoustic metasurface concept has been demonstrated with little effect on the mean flow but greatly suppresses the Mack second mode, it could be considered as one of the most promising control technologies. Absorptive porous coating, as a particular type of acoustic metasurface, was issued to Boeing as a patent in 1999 (US patent number 588471). After decades of development, the US Navy advocated a seed fund in 2019, with the aim of designing, fabricating, characterizing, and testing absorptive porous aeroshell materials that successfully damp the Mack second mode instability to delay BL transition on hypersonic boost-glide weapons during pull-up and glide phases [28]. The program includes three phases (Phases I, II, and III). Phase I focuses on determining the desired porosity characteristics that correspond to BL transition delays in flight regimes of interest. Following the success of the Phase I program objectives, the Phase II plan will refine and validate this new technique. The ability of the materials to delay BL transition while remaining thermally and structurally viable for hypersonic flight will be verified using wind tunnel and arcjet testing. A successful Phase II program will increase the technology readiness level (TRL) from 4 to 6, which will help prepare this technology for a flight test in its operational environment (TRL 7) in Phase III.

1.2. Stabilization mechanisms

It is generally recognized that the Mack second mode behaves like a trapped acoustic mode propagating in a waveguide between the wall and the sonic line; however, with a phase velocity higher than the speed of sound, as illustrated in Fig. 1. The disturbances travel subsonically above the sonic line and outside the BL, and the subsonic wave diminishes exponentially [31]. Each time an acoustic wave is reflected at the sonic line, it changes from a compression wave to an expansion wave, and vice versa. The longitudinal wavelength of the Mack second mode is approximately twice the BL thickness, and its frequency reaches hundreds of kilohertz, corresponding to the ultrasonic band [32, 33]. The Mack second mode exhibits acoustic-wavelike behavior, and therefore, Malmuth et al. [34] proposed a passive porous coating designed to dissipate acoustic energy through the viscous BL inside narrow micropores. In addition to absorptive mechanisms, further studies indicated that the second-mode instability can be stabilized by acoustic manipulations such as phase cancelation [30] and reflection control [35].

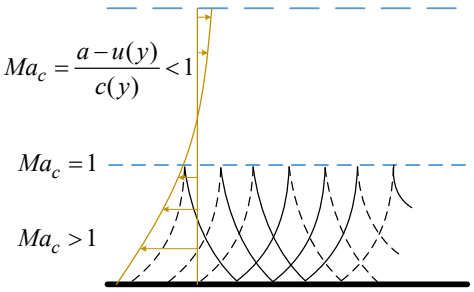

Fig. 1 Acoustic modes trapped in a relative supersonic region where the convective Mach number Ma_c >1 is stationary in this frame of reference (adapted from Morkovin Ref. [29]). Here, $u(y)$and $c(y)$ denote the local speed of flow and sound, respectively, and a denotes the disturbance phase speed [30].

In the natural BL transition, the first mode always coexists with the Mack second mode. The first mode is observed to be slightly destabilized by the presence of a porous coating [19, 36]. Therefore, the first mode may now be more significant in the transition process. The first mode is an extension of the high speeds of the Tollmien–Schlichiting (TS) waves, which represent viscous instability at low Mach numbers. The inviscid nature of the first mode dominates when the Mach number increases; this is because compressible BL profiles contain a generalized inflection point in the BL mean profile where $\partial(\rho\partial u/\partial y)/\partial y = 0$. Here, ρ and u denote the density and streamwise velocity, respectively, and y denotes the axis normal to the wall [19]. This mode is strongly stabilized by wall cooling, suction, and a favorable pressure gradient [20]. Carpenter and Porter [37] proposed a thin perforated sheet stretched over a plenum chamber to stabilize TS waves. The blowing suction caused by the wall fluctuating pressure of the TS mode diminished the Reynolds stress in the near-wall region; then, it stabilized the TS waves along the perforated sheet. Further, they studied the effect of the admittance phase of a perforated sheet on TS waves using the linear stability theory (LST). The growth rate of the TS mode was significantly decreased when the phase approached $\pi/2$. Although this work was conducted in a low-speed incompressible flow, it provides a direction in which the phase of the porous material can possibly affect the first mode. Wang and Zhong [38] studied the stabilization effect of the admittance phase of a porous coating on the first mode in hypersonic BL flows. They found that the destabilization effect in the first mode can be relieved by decreasing the admittance phase of the coating. Tian et al. [39] found that the growth rate of the first mode increased as the admittance phase θ of the coating varied from 0.5π to π; however, the second mode was amplified when θ tended to 0.5π and damped if $\theta \geqslant 0.75\pi$. Further, the stabilization of the Mack second mode, destabilization of the first mode, frequency band broadening, and frequency shifting were promoted by large admittance magnitudes. Based on this principle, Tian et al. [39] theoretically designed a broadband coating that stabilizes the second mode in a wide frequency range with the first mode marginally amplified. Further, Zhao et al. [40] designed a metasurface that decreases the growth rate of the first mode in a Mach 4 flat-plate BL flow. In contrast to the acoustic manipulation mechanisms for the Mack second mode, the reason for the destabilization or stabilization effect of the porous coating phase on the first mode remains unclear.

In certain high-enthalpy wind tunnel experiments and real flight cases, the surface may be relatively cold, i.e., the wall-to-edge temperature ratio is $T_w/T_e < 1$. Bitter and Stepher [41] found that a special supersonic mode emerged at the edge of the BL and traveled outside it. The supersonic mode was oscillatory outside the BL, similar to the "spontaneous radiation of sound" [41-45]. The supersonic mode was considered insignificant in the transition of the high-speed BL owing to the lower amplification rate of this mode compared with that of Mack's subsonic second mode. However, Mortensen [46] recently reported that the rate of growth of the supersonic mode exceeds that of Mack's subsonic second mode in a Mach 20 flow over highly blunt cones. Long et al. [47] proved that the metasurface suppressed the supersonic mode in a highly cooled Mach 6 flat-plate BL flow (Fig. 2). In their work, they applied Doak's momentum potential theory (MPT) [48-52] to explain the stabilization mechanism of the supersonic mode. In

Doak's approach, the momentum density field $\boldsymbol{m}(\equiv\rho\boldsymbol{u})$ is decomposed into the corresponding vortical, acoustic, and thermal components; an energy corollary for the total fluctuating enthalpy (TFE) is derived. This energy corollary helps define the generation and transport of the TFE in the flow field, which provides a causal interpretation of the development of the disturbances. Using MPT, Long et al. [47] found that the positive acoustic source and energy transferred from the vortical component were primary energy producers for acoustic fluxes. Further, the fluctuation energy was transported outward by the acoustic component that led to "sound radiation" in the supersonic mode. In the case of the metasurface, less vortical energy was transported to the critical layer, and therefore, less vortical energy was transformed into acoustic energy. The acoustic energy was exhausted eventually because of the energy loss in the outward transport of the fluctuation energy; the "sound radiation" disappeared from the metasurface. It is interesting to see further interpretations of the stabilization effect of different types of metasurfaces on different modes in the MPT framework because MPT helps reveal the role of different components in the generation and transport of the fluctuation energy and the way in which the fluctuation energy is transferred between components.

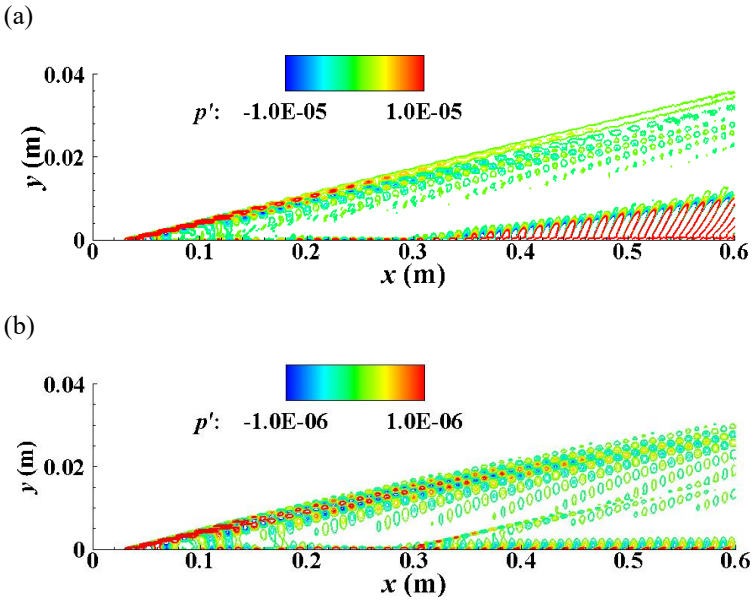

Fig. 2 Instantaneous snapshots of p' (Pa) in the cases of (a) solid wall and (b) a metasurface.

2. Acoustic metasurface classifications

Acoustic metasurfaces are planar metamaterial structures constructed with monolayer or multilayer stacks of subwavelength building blocks, which have significantly broadened the horizon of acoustic wave manipulation from wave-front modulation [53-58], to sound insulation, and absorption [59-61]. The recent emergence of the acoustic metasurface concept has provided more possibilities for controlling the propagation of the Mack second mode.

2.1. Absorptive acoustic metasurface

Compared to the definition of the acoustic metasurface, the aforementioned porous coating (of thickness ~0.1 of the wavelength of the Mack second mode) belongs to the category of an absorptive metasurface. It was first focused on a coating with regular micropores [34]. Fedorov et al. [10] deduced the surface impedance boundary condition to model the acoustic effect of realistic microstructures and applied the LST to investigate the stabilization effect of various inflow conditions and pore shape parameters (Fig. 3). Further, their theoretical finding was verified in the GALCIT T-5 shock tunnel [62] with a 5° half-angle sharp cone at a free-stream Mach number that ranges from 4.59–

6.4. The BL on the half cone covered by the porous surface was mostly laminar, whereas a transition was observed halfway along the other half cone with an untreated solid surface. Given the motivation for a practical coating to be symbiotic with the actual materials of TPS, Fedorov et al. [19] experimentally and theoretically studied the effect of a felt-metal coating with random microstructures on hypersonic BL instabilities (Fig. 4); they showed that this type of porous coating strongly stabilized the second mode and marginally destabilized the first mode. Based on the promising results on porous surfaces with regular and random microstructures and the fact that a majority of TPS materials have random microstructures, the German Aerospace Center (DLR) pioneered the use of carbon–carbon (C/C) (Fig. 5)—an intermediate state of C/C-SiC already employed in hypersonic vehicles [63]—to control the Mack second mode waves. Wind tunnel experiments at Mach 7.5 were conducted; the stabilization of the second mode and an increase in the laminar portion of the BL over the porous surface were observed [64-66]. Wagner et al. [67] optimized the manufacturing process of C/C-SiC to increase its porosity and enhance the stabilization effect on the hypersonic BL.

Based on the abundant investigations of various absorptive acoustic metasurfaces, it is reasonable to suspect that most of porous materials with characteristic pore diameter less than 1mm could stabilize the Mack second mode and delay the hypersonic BL transition. Recently, Zhu et al. [68-70] investigated the stabilization effect of the permeable steel (Fig. 6) on the second mode in a Mach 6 BL flow. It showed this permeable material could effectively weaken the nonlinear interaction and delay the transition, although the second mode grew faster on the material surface. They also found the permeable surface could reduce the pressure-dilatation-induced heat flux by approximately 28%, through the modification of surface sound admittance [12].

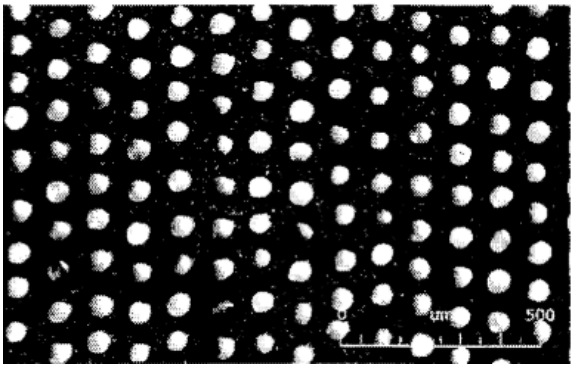

Fig. 3 Microphotograph of porous surface (Porosity ϕ = 0.09, pore diameter d = 0.06 mm, and pore depth h = 0.5 mm) [10].

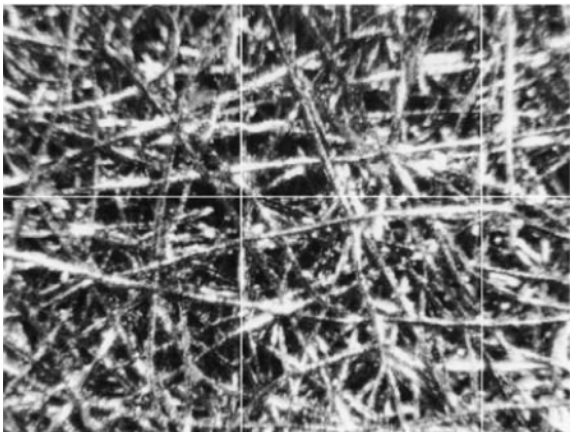

Fig. 4 Microphotograph of felt-metal coating (ϕ = 0.75, averaged d = 0.1 mm, and averaged h = 0.75 mm) [19]

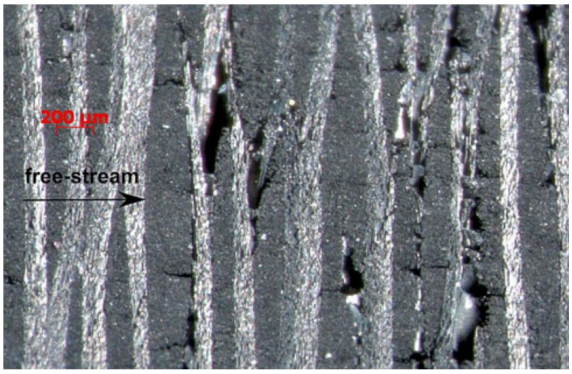

Fig. 5 Microphotograph of the C/C surface ($\phi \approx 0.15$, dominant d = 0.028–0.03 mm, and dominant h = 5–17 mm) [64]

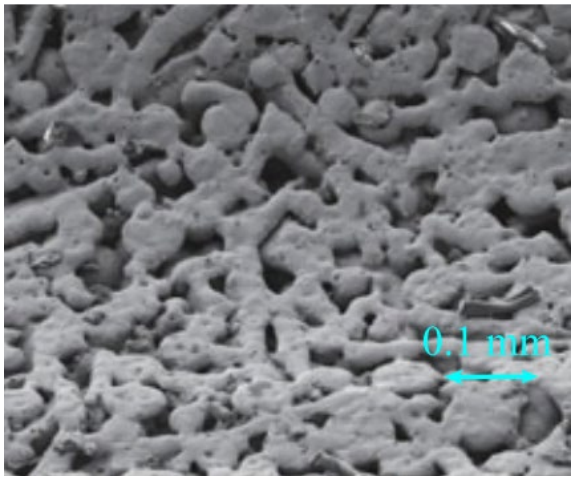

Fig. 6 Microphotograph of porous steel (Air volume ratio = 0.2–0.3 and average aggregate radius ≈ 0.14 mm) [12]

2.2. Impedance-near-zero acoustic metasurface

Matesurfaces could depict specific acoustic characteristics by carefully designing the microstructures. Zhao et al. [30] designed an impedance-near-zero metasurface and showed that even with little damping, the Mack second mode can be greatly suppressed by introducing the near-zero surface acoustic impedance. Fig. 7 shows the acoustic characteristics of the designed impedance-near-zero metasurface without considering the fluid field. The impedance-near-zero metasurface was designed as a rigid surface periodically corrugated with subwavelength slits (lower map in Fig. 7), which resemble the traditional absorptive porous coating [71, 72] (middle map in Fig. 7) but had comparatively shallower cavities. For the impedance-near-zero metasurface, the absolute acoustic pressure field generated by a near-surface point source is extremely weak at the interface $y = 0$, as a result of the out-of-phase behavior between the incident and reflected waves. Sound waves are localized within the central cavity and hardly transmit to neighboring ones, corresponding to a band gap of the surface acoustic wave. This is in stark contrast to the sound field of the absorptive metasurface, wherein most incident waves are absorbed compared with the case of a rigid surface (upper map in Fig. 7), but the acoustic pressure oscillation at the interface remains strong. When the hypersonic BL flow passes the metasurfaces (Fig. 8), the typical two-cell Mack second mode structures [32, 33] at the rigid surface change differently for the two types of metasurfaces. For both types of metasurfaces, the upper cells join the lower part when moving through the metasurface region. The intensity is considerably weakened in the cavities because of the

dissipation effect of the absorptive one (middle map in Fig. 8), whereas the minimum intensity is observed at the surface because of the phase opposition effect for the impedance-near-zero one (lower map in Fig. 8). The impedance-near-zero metasurface divides the mode structures in the cavity and above the surface (lower map in Fig. 8); this inhibits the amplification process of the Mack second mode. In addition, the shallow-cavity design is advantageous for manufacturing and maintenance.

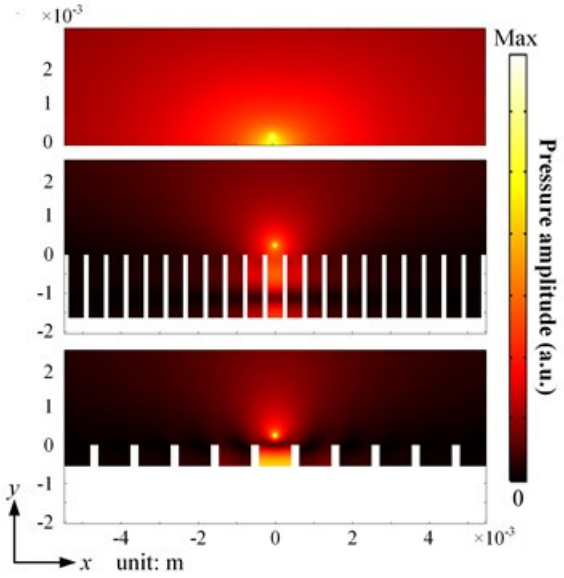

Fig. 7 Simulated absolute acoustic pressure fields for different types of surfaces in the absence of hypersonic fluid flow. Upper: rigid surface; middle: absorptive metasurface with matched impedance; and lower: impedance-near-zero metasurface [30].

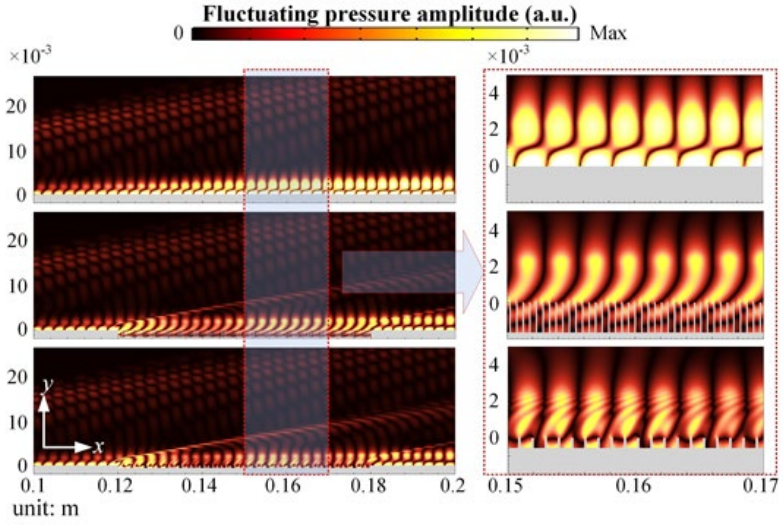

Fig. 8 Fluctuating pressure amplitude contours when a Mach 6 flow passes the metasurface. Upper: rigid surface, middle: absorptive metasurface, lower: impedance-near-zero metasurface (lower), with the corresponding zoom-in views shown in the right column [30].

2.3. Reflection-controlled acoustic metasurface

In addition to the impedance-near-zero metasurface, Zhao et al. [35] proposed a reflection-controlled metasurface for suppressing the Mack second mode by controlling the reflection directions of disturbance waves. The idea of reflection direction control is based on the generalized Snell's law [73,74], i.e., the relationship between the reflection and incident angles in terms of the gradient of the reflection phase along the wall

$$\sin\theta_r - \sin\theta_i = \frac{\lambda}{2\pi}\frac{\mathrm{d}\Phi(x)}{\mathrm{d}x} \tag{1}$$

where θ_r is the reflection angle, θ_i is the incident angle, λ is the wavelength of the incident wave, and $\Phi(x)$ is the reflection phase, which is equal to the reflection coefficient phase when the phase of the incident wave is zero. For second-mode instability waves, a normal incidence can be hypothesized (i.e., $\theta_i = 0$) [71], and therefore, the required θ_r can be achieved by designing the metasurface to produce a constant gradient $\Phi(x)$ along the streamwise direction. Thus, the reflection-controlled metasurfaces comprises periodic slit groups (Fig. 9); each group has N slits with the same half-width b and unit-cell period s but different depths H_i (i =1–N). The reflection phase $\Phi(x)$ can be designed to change linearly from 0 to 2π in each group because of the varied H_i values.

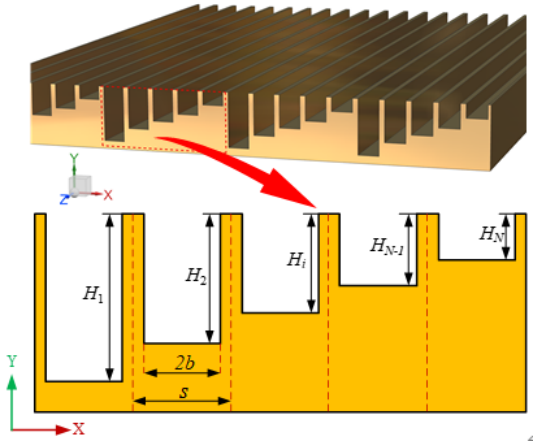

Fig. 9 Schematic of reflection-controlled metasurfaces with subwavelength slits [35]

Zhao et al. [35] subsequently designed three metasurfaces with different reflection angles, namely $\theta_r = \pm 90°$ and $\theta_r = -45°$. As can be seen in **Fig. 10**, the DNS results reveal that the typical "two-cell" structure is divided into several segments when moving through the designed metasurface, and this change is thought to break down the Mack second mode propagation pattern in the BL. It also found that the most effective way to suppress disturbance amplification is to tune reflection wave propagation downstream in the direction parallel to the surface ($\theta_r = 90°$). However, there are too few reflection angles tested in their study to conclude $\theta_r = 90°$ is the optimum angle to stabilize the Mack second mode.

(a)

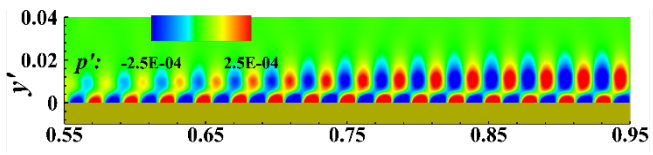

(b)

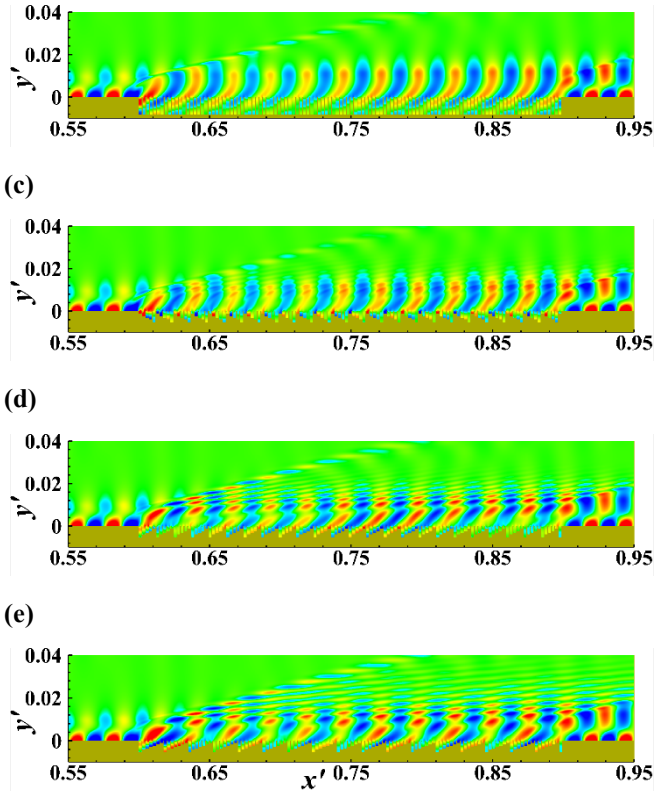

Fig. 10 Fluctuating pressure contours for: a) rigid surface, b) optimized absorptive metasurface, and three reflection-controlled surfaces: c) Case 1: $\theta_r = 90^\circ$, d) Case 2: $\theta_r = -90^\circ$, and e) Case 3: $\theta_r = -45^\circ$. [35]

Besides the long-proposed absorptive acoustic metasurface, the recent artificial impedance-near-zero and reflection-controlled metasurfaces provide two new alternatives for suppressing the Mack second mode. Further, it indicates that the type of porous surfaces with random microstructures such as felt-metal (Fig. 4) and C/C composite (Fig. 5) present not only the absorptive but also other acoustic characteristics when applied to stabilize the hypersonic BL. The manufacturing process can be further optimized to achieve a better stabilization effect. Indeed, the inherent abundant wave manipulation choices through interdisciplinary investigations of metasurfaces and BL flow can benefit the full control of hypersonic BL transition in the future.

3. Mathematical modeling

The stabilization effect of acoustic metasurfaces on hypersonic BL flow is caused by the interaction between their acoustic characteristics and instability waves. In addition to the use of direct numerical simulations of the flow field within microstructures, an acoustic impedance boundary condition of the vertical velocity at the wall ($v_w' = p_w'/Z$) is adopted to model the metasurface. Here, v'_w and p'_w denote the vertical velocity and pressure perturbations, respectively. Z denotes the surface impedance, which is a complex quantity that depends on the properties of the wall material, porosity parameters, mean flow characteristics on the wall surface, and flow perturbation parameters such as wave frequencies and wavelengths. This treatment saves computational resources for numerical simulations and assists in the LST analysis. The influence of the microstructure geometry parameters such as depth, diameter, and porosity can be systematically investigated using the impedance model. It should be noted the applications of the impedance model are independent of the nature of the BL disturbances, e.g., inviscid second mode or viscous TS waves [10]. Gaponov applied the impedance model to investigate the porosity effect on TS waves for subsonic [75,76] and moderate supersonic speeds [77].

3.1. Acoustic metasurface with regular microstructures

Fedorov et al. [10] were the first to develop a formulation of Z for equally spaced cylindrical blind pores by applying the theory of sound wave propagation in thin and long tubes [78-80]. It considered the pore radius and spacing to be much less than the disturbance wavelength, and in this case, the porosity was thought fine enough to avoid disturbing the laminar BL by other mechanisms associated with effective surface roughness. Boundary conditions representing the effect of acoustic metasurfaces are expressed as

$$\begin{aligned} u_{\mathrm{w}} &= 0,\ v_{\mathrm{w}} = Ap_{\mathrm{w}}^{'},\ w_{\mathrm{w}} = 0, \\ T_{\mathrm{w}}^{'} &= Bp_{\mathrm{w}}^{'} \end{aligned} \tag{2}$$

where A ($\equiv 1/Z$) and B represent the sound and thermal admittances, respectively. In Eq. (2),

$$\begin{aligned} A &= -(\phi / Z_0)\tanh(\Lambda h) \\ B &= -\phi(\gamma - 1)Ma^2 T_w J_2(k_t) / J_0(k_t) \end{aligned} \tag{3}$$

where ϕ is porosity, h is the porous-layer thickness, Z_0 is characteristic impedance, Λ is the propagation constant, J_0 and J_2 are Bessel functions, and k_t measures the ratio of the tube radius to the thermal BL thickness on the tube surface [10]. Z_0 and Λ are calculated using the transmission line formalism [79, 80], and B can be assumed to be zero because the temperature perturbations on the metasurface weakly affect the disturbance growth rate after investigations [10]. The same analytical solution of Z_0 and Λ can be obtained in terms of the complex dynamic density $\tilde{\rho}$ and compressibility $\tilde{C}$ [81], which is more convenient for the analysis of acoustic disturbances in randomly porous materials and is widely applied in subsequent research. As indicated in Eq. (3), A and B are originally deduced for a single cylindrical pore and they neglect the interactions among neighboring pores. The integral acoustic characteristics of the metasurfaces are evaluated by multiplying ϕ.

Under wind-tunnel conditions, the fluid density is relatively small, and the rarefaction effects inside the pores may be important. Maslov [82] stated that the rarefaction effect would make metasurfaces more transparent with respect to the disturbance, and this would lead to the stronger stabilization of the second mode. As the Knudsen number increased to Kn = 0.588, the growth ratio of the Mach second mode calculated by the LST decreased by 15–20% considering the rarefaction effect. Relatively comprehensive rarefaction models for regular metasurfaces of various cross-sectional microstructures (circle, rectangular, triangular, and slit) were proposed by Kozlov et al. [83]. All these models ignore the end effects associated with the scattering of incoming acoustic waves at the cavity/pore mouth. Further, there is no coupling between disturbances from neighboring cavities or pores, and this may not be true for closely spaced cavities. To consider the coupling between disturbances from neighboring cavities, Brès et al. [72] hypothesized a slip velocity at the wall with expressions such as $u_w^{'} = f(v_w^{'}, p_w^{'})$ for the LST analysis. Nevertheless, they indicated that this boundary condition should be further studied and refined because of the large number of fitting parameters. Zhao et al. [84] considered the high-order diffracted modes of plane ultrasonic acoustic waves impinging on metasurfaces with microslits (Fig. 11); they proposed a model that incorporated mutual coupling among neighboring cavities, which improves the accuracy of the predicated acoustic characteristics. The model is expressed as

$$R_0 = 1 + \frac{2j\tan(k_h h)\frac{\rho_w}{\tilde{\rho}}\phi\frac{k_h}{k_0}}{1 - j\tan(k_h h)\frac{\rho_w}{\tilde{\rho}}\phi\sum_{r=-\infty}^{+\infty}\frac{k_h}{\sqrt{k_0^2 - (\frac{2r\pi}{s})^2}}S_r^2}. \quad (4)$$

$$Z = \frac{1}{A} = \rho c\frac{R_0 + 1}{R_0 - 1}$$

where $S_r = (2b)^{-1}\int_{-b}^{b} e^{jk_x^{(n)}x}dx = sinc(k_x^{(n)}b)$ represents the overlap integral between the rth-order diffracted mode and the fundamental mode inside the cavity [84]. The proposed model shows an improvement in the accuracy of the predicted reflection frequency, and it successfully reproduces a coupling mode induced by interactions between waves scattered from adjacent cavities. Further, the limitation of the model was declared: the incident wavelength should be much larger than the cavity period $\lambda >> s$. When the designed period s increases to the same order as wavelength λ, the interaction of the scattered waves at the metasurface becomes strong, and this greatly decreases the absorption performance. In particular, if this model neglects all higher-order diffracted modes and let the porosity ϕ approach zero (the local oscillation inside each cavity is independent), Eq.(4) is reduced to the one proposed by Kozlov et al. [83]:

$$R_0 = \frac{1 + j\tan(k_h h)\frac{\rho_w}{\tilde{\rho}}\phi\frac{k_h}{k_0}}{1 - j\tan(k_h h)\frac{\rho_w}{\tilde{\rho}}\phi\frac{k_h}{k_0}} \quad (5)$$

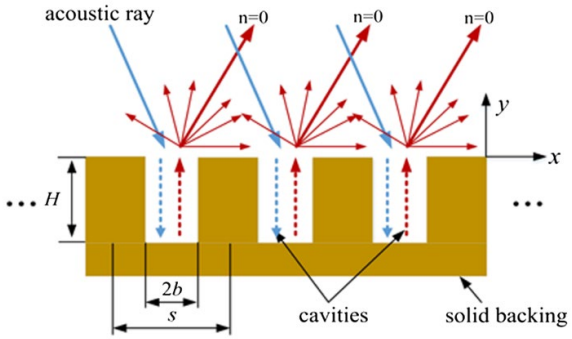

Fig. 11 Schematic of the reflection of acoustic waves from equally spaced two-dimensional cavities [84].

Zhao et al. [85] further extended the plane wave expansion method to derive impedance models for metasurfaces with 3D pores of circular and square cross sections, which are considered more practical for engineering applications. Sandham and Lüdeke [86] used the LST to reveal that the stabilization effects of metasurfaces with different slit or pore shapes that could be collapsed in good agreement for the same hydraulic diameter d_h ($d_h = 4A_p / C$, where A_p represents the slit or pore area and C denotes the circumference). In line with this, Zhao et al. [85] confirmed the consistency of the acoustic characteristics provided they had the same d_h, ϕ, and depth H (Fig. 12).

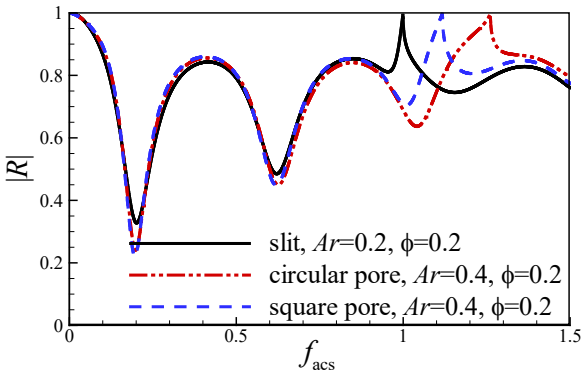

Fig. 12 Comparison of the reflection coefficient amplitude distributions for slits or pores with the same hydraulic diameter [85].

3.2. Acoustic metasurface with random microstructures

Since the majority of TPS materials have random microstructures, many studies were performed to model the acoustic characteristics of this type of metasurface [19, 87-91]. The formations resemble those in Eq. (3). However, there is no rigorous theory to obtain the exact complex dynamic density $\tilde{\rho}$ and the complex dynamic compressibility $\tilde{C}$. Delany and Bazley [92] provided empirical relationships for $\tilde{\rho}$ and $\tilde{C}$ for fibrous absorbent materials that are widely used in various applications such as sound attenuation in dust, room acoustics, and transmission loss through walls. Fedorov et al. [19, 87] derived semi-empirical relations for a felt-metal material (Fig. 4). Their model requires additional parameters because of their random nature, including tortuosity a_∞, flow resistivity σ, and characteristic pore size r_p. a_∞ is equivalent to the structure-form factor [93] and it is coupled with the dynamic density $\tilde{\rho}(\omega)$ as $a_\infty = \lim_{\omega\to 0}\tilde{\rho}(\omega)$; it adopts a value of unity. Further, σ should be measured and fitted in the laboratory, for example, in an impedance tube experiment; σ has a large measurement uncertainty of up to 12.6%, although this uncertainty weakly affects the second-mode amplification [19]. For isotropic porous materials, r_p can be expressed as $r_p = s_h\sqrt{8\mu a_\infty/\sigma\phi}$, where s_h denotes the dimensionless shape factor [94]. The felt-metal is highly anisotropic, and Fedorov et al. [19, 87] treated r_p as a hydraulic radius. They considered an average statistical elementary cell simulating the topology of the felt metal microstructure (Fig. 13), and they represented r_p as a function of the porosity ϕ and fiber diameter d, which can be measured experimentally.

$$r_p = \frac{\pi d}{2(1-\phi)(2-\phi)}. \tag{6}$$

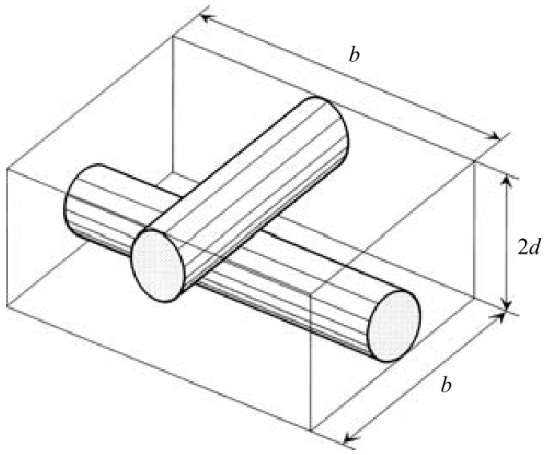

Fig. 13 Elementary cell of the felt-metal microstructure; $b \times b \times 2d$ parallelepiped including two adjoining sections of fibers with diameter d [19].

In contrast to the above analytical impedance models for metasurfaces with regular and felt-metal microstructures, the German DLR and Purdue University adopted the inverse Helmholtz solver (IHS) to estimate the C/C impedance. The IHS is a computational methodology that allows the evaluation of the spatial distribution of acoustic impedance at the open surface of an arbitrarily shaped cavity for a given frequency [89-91]. In the application, a high-resolution image of the C/C block (Fig. 14 (a)) auto-detects the edges of large surface cavities depending on the grayscale value (Fig. 14 (b)), makes an automatic approximation to a rectangular slot or a cylindrical pore based on the extent of the pores in each direction, and meshes their volumes to serve as an input geometry to the HIS (Fig. 14 (C)). Finally, the broadband impedance of each individual surface cavity is evaluated. These impedances are combined to yield the effective surface-averaged impedance for the C/C block.

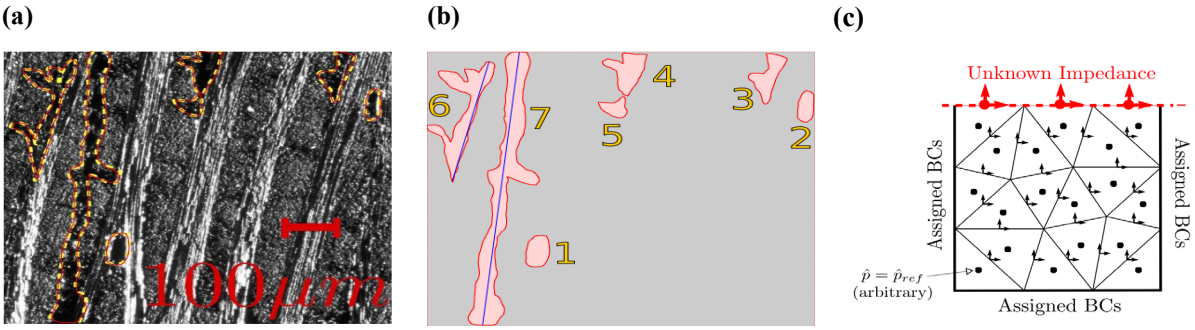

Fig. 14 Inverse Helmholtz solver procedure used to calculate the impedance of cavities typical of blind-hole porous surfaces, (a) high-definition image of the C/C block, (b) detected large cavity edges, and (c) simplified two dimensional computational setup [90, 91].

Sousa et al. [95] compared analytical impedance models and the IHS method in the prediction of the acoustic characteristics of C/C materials at various base pressures. The analytical impedance models used the homogeneous absorber theory (HAT) [96] and the felt-metal model proposed by Fedorov et al. [19, 87]. Fig. 15 shows that the IHS can predict a consistent absorptive coefficient with the experiment by Wagner et al. [91], especially in an environment of lower base pressure. When the test base pressure increases or the incident wave frequency increases, the prediction accuracy of the IHS degrades significantly. The discrepancy in the IHS results was attributed to the underestimated volume porosity, given that only a limited selection of the largest visible pores in Fig. 14 (a) was used for the direct

impedance estimate [95]. Compared to the HAT model, the felt-metal model had a higher accuracy and showed a better tendency with the experiment.

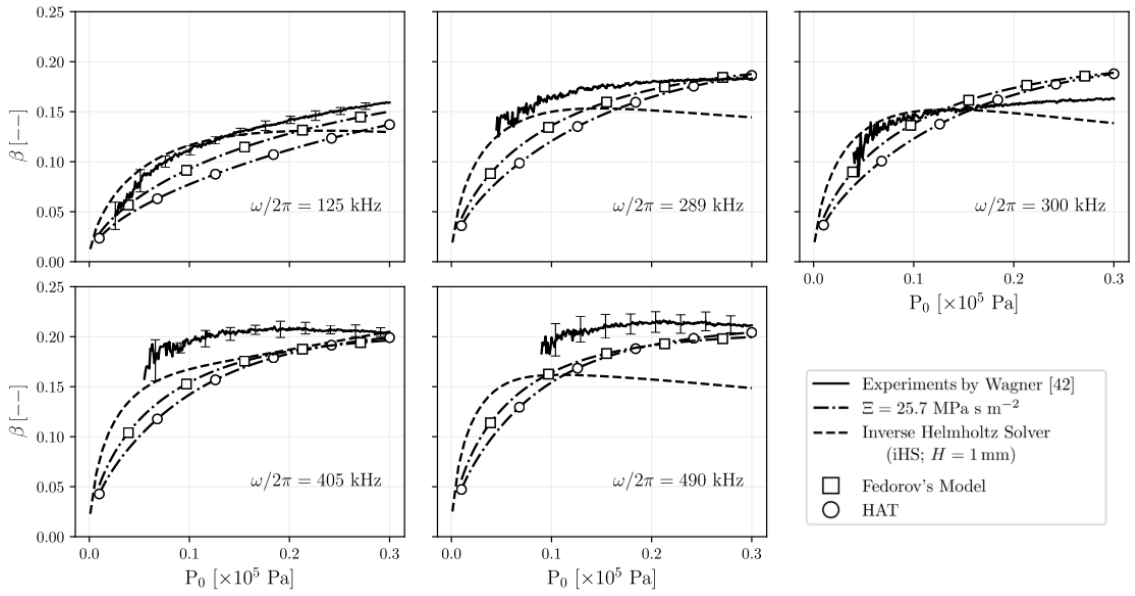

Fig. 15 Comparison of measured and predicted absorption coefficient β for the classical C/C vs. base pressure [95].

4. Research progress in the past two decades

In the past two decades, many studies have been performed to study the stabilization effect of acoustic metasurfaces on hypersonic BL flows using LST, DNS, or wind tunnel experiments. With the acoustic impedance model implemented as the boundary condition, the LST can predict the growth ratio of any single mode affected by metasurfaces in the linear stage of the BL transition. In addition to the use of the impedance model to save computational resources, direct numerical simulations of the flow field within the microstructures can provide more information on the interaction mechanisms. The wind tunnel experiments can directly prove the stabilization effect on the unstable modes and help evaluate the delay performance by measuring the transition onset locations. Table 1 reviews and summarizes the major achievements that have been conducted theoretically, numerically, and experimentally.

Table 1 Summary of theoretical, numerical, and experimental progresses on the metasurface transition control technology

Primary theoretical studies				
Ref.	Metasurface type	Model	Method	Main points
Fedorov et al. [10] Wartemann et al. [98]	Regular: Equally spaced cylindrical micropores	Mach 6, flat-plate	LST	Parametric study on the effect of pore diameter, depth, and porosity
Brès et al. [71, 72, 99]	Regular: Equally spaced microslits	Mach 6, flat-plate	LST	Report the cancellation/reinforcement working regime of metasurfaces
Zhao et al. [30]	Regular: Equally spaced micro-slits	Mach 6, flat-plate	LST	Report the impedance-near-zero metasurface

Zhao et al. [84]	Regular: Equally spaced micro-slits	Mach 6, flat-plate		Propose the numerical optimization method for absorptive metasurfaces
Fedorov et al. [19] Tritarelli et al. [100]	Random: Felt-metal	Mach 6, sharp cone	LST	Report the stabilization of Mack second mode and destabilization of first mode
Wartemann et al. [101]	Random: C/C material	Mach 7.5, sharp cone	LST, e^N	Suggest the impedance model for the LST analysis of the C/C material
Stephen and Michael [36]	Regular: Equally spaced cylindrical micropores; Random: Mesh layers [102]; Random: felt-metal	Mach 5.3, sharp cone	LST	Demonstrate the destabilization of the nonaxisymmetric first mode
Tian et al. [39]	Regular: Gradient micro-slits	Mach 4, flat-plate	LST	Propose a metasurface to suppress the second mode without amplifying the first mode distinctly
Zhao et al. [40]	Regular: Gradient micro-slits	Mach 4, flat-plate	LST	Propose a metasurface to suppress the first mode
Xu et al. [103]	Regular: Equally spaced cylindrical micropores;	Mach 4.5, flat-plate	SIT	Investigate the stabilization on secondary instability

Primary numerical studies

Ref.	Metasurface type	Model	Method	Main points
Egorov et al. [105]	Regular: Equally spaced cylindrical blind micropores	Mach 6, flat-plate, sharp cone; Mach 5, compression corner	DNS_BC	Confirm robustness of the metasurface stabilization concept
Wang and Zhong [106-108]	Random: Felt-metal	Mach 6, flat-plate	DNS_BC	Emphasize on the effect of metasurface location and the first-mode destabilization
Wang and Zhong [109]	Regular: Equally spaced microslits; Random: Felt-metal	Mach 6, flat-plate	DNS_BC	Compare the stabilization efficiencies between the regular one and the felt-metal one
Sousa et al. [111] [115]	Random: C/C material	Mach 7.5, sharp cone	DNS_TDIBC	Attempt to simulate the full transition along the metasurface
Chen and Scalo [116]	A single-pole Helmholtz oscillator	Mach 1.5, 3.5, and 6: Channel	DNS_TDIBC	Investigate the effect of a wall with complex impedance on the supersonic/hypersonic flows.
Brès et al. [72, 118, 120]	Regular: Equally spaced microslits	Mach 6, flat-plate	TDNS	Demonstrate the cancellation/reinforcement working regime of metasurfaces
Sandham and Lüdeke [86] Fedorov [117]	Regular: Equally spaced microslits, equally spaced rectangular micropores	Mach 6, flat-plate	TDNS	Confirm the consistence with LST predications
Tulio and Sandham [121]	Regular: Equally spaced square micropores	Mach 6, flat-plate	TDNS	Report the stabilization of primary and secondary instabilities, and destabilization of first mode
Hader et al. [122, 123]	Regular: Equally spaced square micropores	Mach 6, flat-plate	TDNS	Focus on the effect of metasurfaces on the nonlinear regime of transition
Zhu et al. [124]	Regular: Equally spaced square micropores	Mach 6, flat-plate	SDNS	Compare the stabilization effect of different pore distributions
Zhao et al. [119]	Regular: Equally spaced microslits	Mach 6, flat-plate	SDNS	Systematically investigate the metasurface effect on the outflow

				fields, accuracy of the theoretical model, and the location effect
Zhao et al. [30, 35]	Regular: Microslits	Mach 6, flat-plate	SDNS	Demonstrate the stabilization effect of the impedance-near-zero and reflection-controlled metasurfaces
Guo et al. [125]	Regular: Equally spaced slits	Mach 6, flat-plate	SDNS	Investigate the stabilization effect of relatively large cavities

Primary experimental studies

Ref.	Metasurface type	Model	Tunnel	Main points
Rasheed et al. [62]	Regular: Equally spaced cylindrical micropores	Mach 5, sharp cone	GALCIT T-5 shock tunnel	Verify the metasurface transition control concept
Fedorov et al. [126]	Regular: Equally spaced cylindrical micropores	Mach 6, sharp cone	ITAM T-326 blowdown wind tunnel	Compare the metasurface stabilization effect with LST predications
Fedorov et al. [19]	Random: Felt-metal	Mach 6, sharp cone	ITAM T-326 blowdown wind tunnel	Compare the metasurface stabilization effect with LST predications
Maslov et al. [127]	Random: Felt-metal	Mach 12, sharp cone	ITAM AT-303 high-enthalpy wind tunnel	Investigate the transition onset under varied inflow Reynolds numbers, and make comparisons with e^N predications
Lukashevich et al. [128, 129]	Random: Three layers of a nylon mesh	Mach 5.8, sharp cone	Transit-M hypersonic short-duration wind tunnel	Systematically investigate the effect of the metasurface length and location
Wagner et al. [64-67]	Random: C/C material	Mach 7.5, sharp cone	High enthalpy shock tunnel Göttingen	Report the stabilization effect and transition delay performance
Chokani et al. [130] Bountin et al. [131]	Regular: Equally spaced cylindrical micropores	Mach 6, sharp cone	ITAM T-326 blowdown wind tunnel	Bispectral analysis of the metasurface effect on the nonlinear regime of transition
Zhu et al. [68-70]	Random: Permeable steel materials	Mach 6, sharp cone	Peking University hypersonic wind tunnel	Clarify the stabilization mechanisms

DNS_BC: DNS with the metasurface modeled as an impedance boundary condition for a single-frequency disturbance [Eq. (10)]; DNS_ TDIBC: DNS with the metasurface modeled as a time-domain impedance boundary condition for broadband disturbances [Eq. (11)], TDNS: temporal DNS, SDNS: spatial DNS.

4.1. Theoretical analysis

LST assumes that the flow variables $q = [\rho, \rho u, \rho v, \rho w, e]^T$ can be decomposed into $q = \overline{q} + q'$, where $\overline{q}$ denotes the mean flow and q' denotes the perturbation field. Then, the Navier–Stokes (N–S) equations are linearized by neglecting the high-order terms in q'. With the assumption that the mean flow is parallel or quasi-parallel, the mean

flow velocity and temperature profiles are functions of y (normal distance from the wall), which is a wavelike perturbation solution that can be written as

$$q'(x,y,t) = \text{Real}\left\{\hat{q}(y)\exp\left[i\left(\alpha x + \beta z - \omega t\right)\right]\right\} \tag{7}$$

where $\hat{q}(y)=[\hat{u},\hat{v},\hat{p},\hat{T}]^T$ is a complex amplitude function, α and β are the dimensionless wavenumbers in the x- and z-directions (streamwise and spanwise directions), and ω denotes the angular frequency. For the spatial stability problem in two-dimensional (2D) BL flows, the spanwise wavenumber $\beta = 0$ and angular frequency ω is real, whereas α denotes a complex eigenvalue, $\alpha = \alpha_r + i\alpha_i$. If $\alpha_i < 0$, the flow is unstable with a spatial growth rate α_i and streamwise wavenumber α_r. The local phase velocity is defined as $a = \omega/\alpha_r$ [97]. The boundary conditions are given by

$$\begin{aligned} &\hat{u} = \hat{T} = 0, \ \hat{v} = A\hat{p}, \quad && y = 0 \\ &\hat{u} = \hat{v} = \hat{T} = 0, && y \to \infty \end{aligned} \tag{8}$$

Fedorov et al. [10] conducted parametric studies on the stabilization effect of an acoustic metasurface with equally spaced cylindrical blind micropores. It was found that deep pores (pore depth is approximately five diameters) with a relatively small radius could stabilize the Mack second mode in a wide frequency band at various Reynolds numbers. The maximum growth rate gradually diminished as the porosity increased. As the depth increased, the growth rate decreased to a limit. Further, they also indicated that an optimal depth existed at which the disturbance waves reflected from the pore bottom were in counter phase with the BL disturbance, i.e., the pores became acoustic resonance. Wartemann et al. [98] confirmed that the maximum growth rate of the second Mack mode decreased to a limit as the depth became larger than approximately five pore diameters in the LST analysis of the Mach 6 BL flow. Further, an optimal depth was found, and it was considerably smaller than the limit pore depth (Fig. 16).

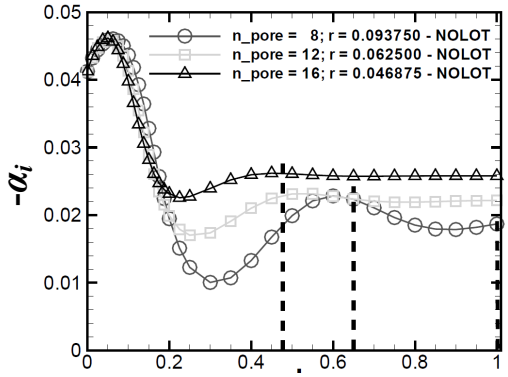

Fig. 16 Growth rate -α_i against pore depth H at various pore radius r in a Mach 6 BL flow. The dashed line shows the limit-pore depth that is about five times of the pore diameter [98].

Brès et al. [71, 72, 99] considered metasurfaces operating in attenuative regimes where pores were relatively deep and cancellation/reinforcement regimes with alternating regions of local minima and maxima of the metasurface acoustic absorption depending on the disturbance frequency. As shown in Fig. 17, the stabilization effect is considerable when the metasurface operates in the cancelation regime. Further, in this best-case scenario, the pores are shallower with the added convenience of manufacturing and maintenance. With the hypothesis that the maximum absorption occurs when the reflection from the pore bottom and metasurface is in opposition to the phase, they presented a simple model to predict the frequencies of the minimum reflection coefficient [71, 99]

$$\frac{fH}{a_{\mathrm{w}}} = (2n-1)/4 \tag{9}$$

where f denotes the disturbance frequency, H represents the pore depth, a_{w} denotes the sound velocity at the wall, and n denotes an integer with n = 1, 2, 3, which leads to specific frequencies of 0.25,0.75, and 1.25 that correspond to the local minima of the reflection coefficient [Fig. 17(a)].

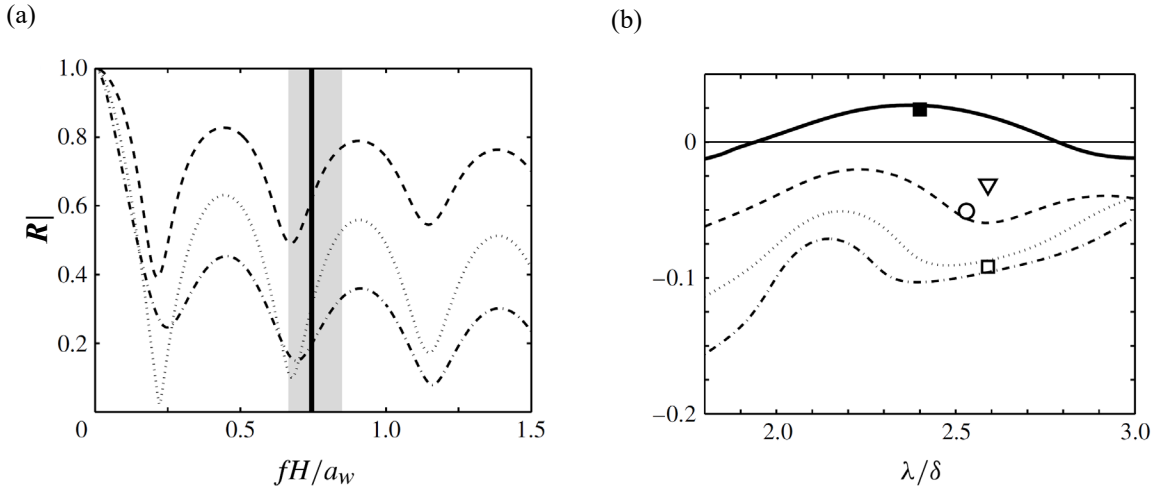

Fig. 17 Performance improvement for the metasurface in the cancellation regime: Ma_∞ = 6, Re_δ = 31300, cavity aspect ratio Ar = 0.12, and porosity ϕ = 0.2 (dashed line), ϕ = 0.48 (dotted line), and ϕ = 0.8 (dot-dashed line). (a) Reflection coefficient amplitude from theory. The grey shaded area corresponds to the frequencies of the unstable modes and the vertical thick line represents the frequency of the most unstable mode. (b) A linear growth rate from LST for the metasurfaces and the rigid flat plate (thick line) [72]

Furthermore, Zhao et al. [30, 84] proposed a numerical solution to obtain the minimum $|R|$ by carefully selecting the geometrical parameters of the microslits in Eq. (4) to achieve $|R| = 0$ directly. The optimization was achieved by solving Eq. (3) with program loops in the following order: loop 1: $0.2 \leqslant \phi \leqslant 0.8$, loop 2: $0.06 \leqslant Ar \leqslant 1.5$, and loop 3: $0 < f_{\mathrm{acs}} < \min(\phi/Ar, 2.0)$, where $Ar = 2b/H$ was the aspect ratio and $f_{\mathrm{acs}} = fH/c$ was the normalized frequency. These parameters span the range of interest for practical applications [72] and ensure the accuracy of Eq. (4). With this method, the obtained $|R|$ at a given frequency f can be optimized close to zero, and the second mode can be suppressed to the maximum extent using the sound absorptive mechanisms of the metasurfaces. The optimized "cancellation" design can only prominently suppress the Mack second mode at around the designed frequency; however, its performance quickly deteriorates compared to that of the conventional "deep-pores" design (Fig. 8). Equation (4) indicates that the metasurface impedance matches the background impedance when $|R| = 0$. Under this condition, the metasurface completely dissipates acoustic disturbances; however, it is not the only choice to stabilize the acoustic Mack second mode. Zhao et al. [30] showed that the growth rate continued to decrease as the impedance became smaller than the background impedance, i.e., the metasurface tended to become nondissipative, and yet, the Mack second mode was effectively suppressed in an even better manner. They attributed this phenomenon to the minimized acoustic pressure perturbation at the antinode of the Mack second mode and designed the impedance-near-zero metasurface as a practical realization.

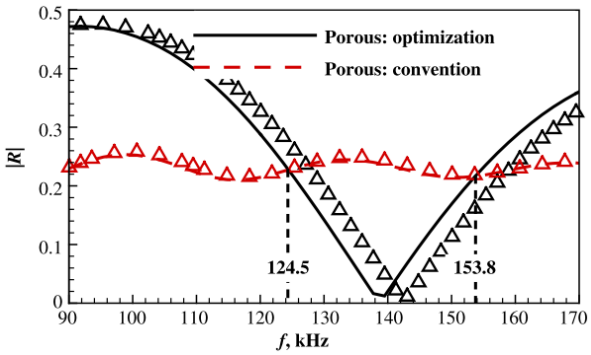

Fig. 18 Comparison of reflection coefficient distributions in broadband frequencies ($Ma_\infty = 6$; $Re_\infty = 10.5 \times 10^6$ m^{-1}; and the designed frequency for the optimized metasurface is 138.74 kHz) [84].

In the LST analysis of the stabilization effect of the felt-metal microstructures [19, 100], the strong stabilization of second-mode disturbances and the minor destabilization of the first-mode disturbances were observed. The second mode was shifted to lower frequencies, which is in accordance with the results for metasurfaces with regular microstructures [10]. Wartemann et al. [101] compared the effectiveness of different impedance boundary conditions to model the stabilization effect of C/C materials, and they found that the LST based on the felt-metal model [19, 87] delivered the best agreement with the experiments. Stephen and Michael [36] theoretically considered the effect of various metasurfaces on the first mode of a hypersonic BL on a sharp slender cone; they found that the metasurface significantly destabilized nonaxisymmetric modes. Tian et al. [39] used the LST to investigate the stabilization effect of the metasurface admittance phase θ and magnitude $|A|$ systematically for broadening the stabilization range of unstable modes; they found that the stabilization of the Mack modes was closely dependent on phase θ. Further, the corresponding stabilization or destabilization effect was intensified by an increase in the admittance magnitude $|A|$. The first mode is marginally stabilized if θ approaches 0.5π and is greatly destabilized near $\theta = \pi$. In contrast, the second mode is restrained when $\theta \geqslant 0.75\pi$ and amplified as θ approaches 0.5π. Following the theoretical analysis, they designed a metasurface with gradient microslits to suppress the second mode across a wide frequency band without amplifying the first mode distinctly in a Mach 4 flat-plate BL flow. Considering that the first mode is the dominant instability that induces a transition in the supersonic condition, Zhao et al. [40] further theoretically proposed a metasurface to suppress the first mode in a wide frequency band. Although the LST results prove that the acoustic metasurface can stabilize the first mode, the roughness effect is ignored in the LST analysis, and it can otherwise excite the first mode. Recently, Xu et al. [103] used the floquet-based secondary instability theory (SIT) [104] to investigate the stabilization effect of acoustic metasurfaces on the secondary instability. They found that there are no strongly preferred interaction modes dominating the secondary instability that corresponds to different amplitudes of the primary Mack mode disturbances affected by the porosity parameters. This finding is in contrast with that of the smooth wall. Further, they found that the suppression of the fundamental mode became more efficient with a larger pore size or porosity.

4.2. Numerical simulations

Generally, there are two numerical strategies to directly simulate the BL flow that interacts with the acoustic metasurfaces. One strategy adopts the impedance boundary condition, similar to the LST ($v_w' = p_w'/Z$). The impedance $Z(\omega)$ is originally defined in the frequency domain and should be solved in the time domain to study the disturbance propagation over the acoustic metasurface. In the coupling with the (N–S) equations for a single disturbance frequency ω, this relationship is written as [105]

$$v_{\mathrm{w}} = p'_{\mathrm{w}}\,\mathrm{Real}(1/Z) - \frac{1}{\omega}\frac{\partial p'_{\mathrm{w}}}{\partial t}\,\mathrm{Imag}(1/Z) \tag{10}$$

Egorov et al. [105] performed the DNS of the flows over a flat plate, sharp cone, and compression corner at freestream Mach numbers 5–6, which use the impedance model of the metasurface that comprises equally spaced cylindrical blind micropores [10]. In the flat-plate BL flow, they compared the fluctuating wall pressure with the LST and showed a consistent result. The coating end effects that are associated with the discontinuity of the boundary conditions at the juncture between the solid and the metasurface were found to be localized over 2–3 disturbance wavelengths and can be neglected. Further, the effect of the metasurface on receptivity to acoustic disturbances was studied. The metasurface weakly affected the acoustic disturbances and initial amplitudes of the BL modes, whereas it strongly suppressed the second-mode amplification. The compression corner flow showed that the metasurface weakly affected high-frequency disturbances in the separation region and strongly stabilized them in the reattached flow. Their numerical studies confirmed the robustness of the acoustic metasurface stabilization concept. Using the felt-metal impedance model [19], Wang and Zhong [106-108] studied the stabilization of a Mach 5.92 flat-plate BL using local sections of the metasurface with an emphasis on the effect of metasurface location and first-mode destabilization. They found that the disturbances were destabilized or stabilized when the metasurface was located upstream or downstream of the synchronization point. The synchronization point is the streamwise location where the phase speed of mode *F* synchronizes with that of mode *S* at a particular frequency of disturbance. In addition, they compared the stabilization efficiencies of two types of metasurface impedance models at approximately the same porosity, i.e., the regular model comprising the microslits and felt-metal one [109], and they concluded that the regular metasurface was less efficient in stabilizing the second mode and tended to destabilize the first mode to a smaller extent.

As mentioned previously, Eq.(10) is applicable only to a single disturbance frequency. It can deal with the metasurface stabilization effect on the most unstable mode, but fails to simulate the response of the broadband disturbances in the real flight or most wind tunnel conditions. Mathematically, the time-domain equivalent of $Z(\omega)$ can be derived by taking its inverse Fourier transform. However, the inverse Fourier transform of the frequency-domain impedance boundary condition leads to a convolution integral. The computation of the convolution integral is time-consuming, especially when coupling with DNS studies [110]. If the impedance can be represented by a sum of certain special functions, the evaluation of the convolution can be performed in a simple systematic manner. Therefore, the metasurface stabilization effect on the broadband instabilities, even in the full transition process and turbulence, can be evaluated. In 2019, Sousa et al. [111] conducted the DNS of a spatially developing hypersonic BL flow over a sharp cone at Mach 7.5. They developed the time-domain impedance boundary conditions (TDIBC) to model the acoustic response of a C/C metasurface to a broadband disturbance. The TDIBC application requires that the acoustic impedance be specified as a set of complex poles and residues representing a superposition of causal second-order oscillators [112-114]. These poles and residues were obtained by fitting the wall softness coefficient that corresponds to the evaluated broadband acoustic impedance from the IHS (Section 3.2).

$$\hat{S}(\omega) = \hat{R}(\omega) + 1 = \frac{2}{1 + Z_*(\omega)} \approx \sum_{k=1}^{n_0}\left[\frac{\mu_k}{s - p_k} + \frac{\tilde{\mu}_k}{s - \tilde{p}_k}\right] \tag{11}$$

where $\hat{S}$ and $\hat{R}$ denote the respective softness and reflection coefficients, respectively; Z_* denotes the nondimensional impedance; n_0 denotes the number of oscillators; μ_k and p_k represent the k-th residue and k-th pole of $\hat{S}$, respectively; $s = j\omega$; and the superscript ~ denotes the complex conjugate. The fitting residues and poles are provided to predict the next time ($t+\Delta t$) reflected wave from the metasurface, and the incident wave is evaluated by extrapolating the value of the incoming wave in time based on the truncated Taylor series expansion in space [114]. The fluctuating wall-normal velocity at $t+\Delta t$ is given by

$$v'(t+\Delta t)=\frac{1}{2}\left[v^{+}(t+\Delta t)+v^{-}(t+\Delta t)\right] \tag{12}$$

where v^{+} denotes the incident wave and v^{-} denotes the reflected wave. Using the TDIBC method, Sousa et al. [115] conducted a 3D DNS of transition to turbulence in a hypersonic sharp cone flow with a C/C metasurface. The simulation was started at the onset of transition; however, it collapsed after the appearance of shocklets inside turbulent spots during the transition owing to the low robustness of their numerical scheme. However, the effectiveness of the C/C metasurface in attenuating second-mode waves was demonstrated again. Further, the impedance boundary was reactive to the 3D overlying transitional turbulent flow, which resulted in an effective decrease in the wall heat flux (Fig. 19). In addition, they indicated that the impedance boundary may not be applicable for turbulence flow because turbulent structures exhibit smaller scales in the order of the metasurface microstructure. Recently, Chen and Scalo [116] investigated the effect of an isothermal wall with complex impedance on the compressible turbulent channel flow up to the bulk Mach number 6 via the TDIBC. The results indicated that the wall-shear stress was enhanced because of the new emerging streamwise-travelling waves which entail high–low alternating wall pressure patterns. The resonating frequency and resistance values applied in their research are not necessarily the case in real applications, and the revealed wave structures need to be confirmed via experiments.

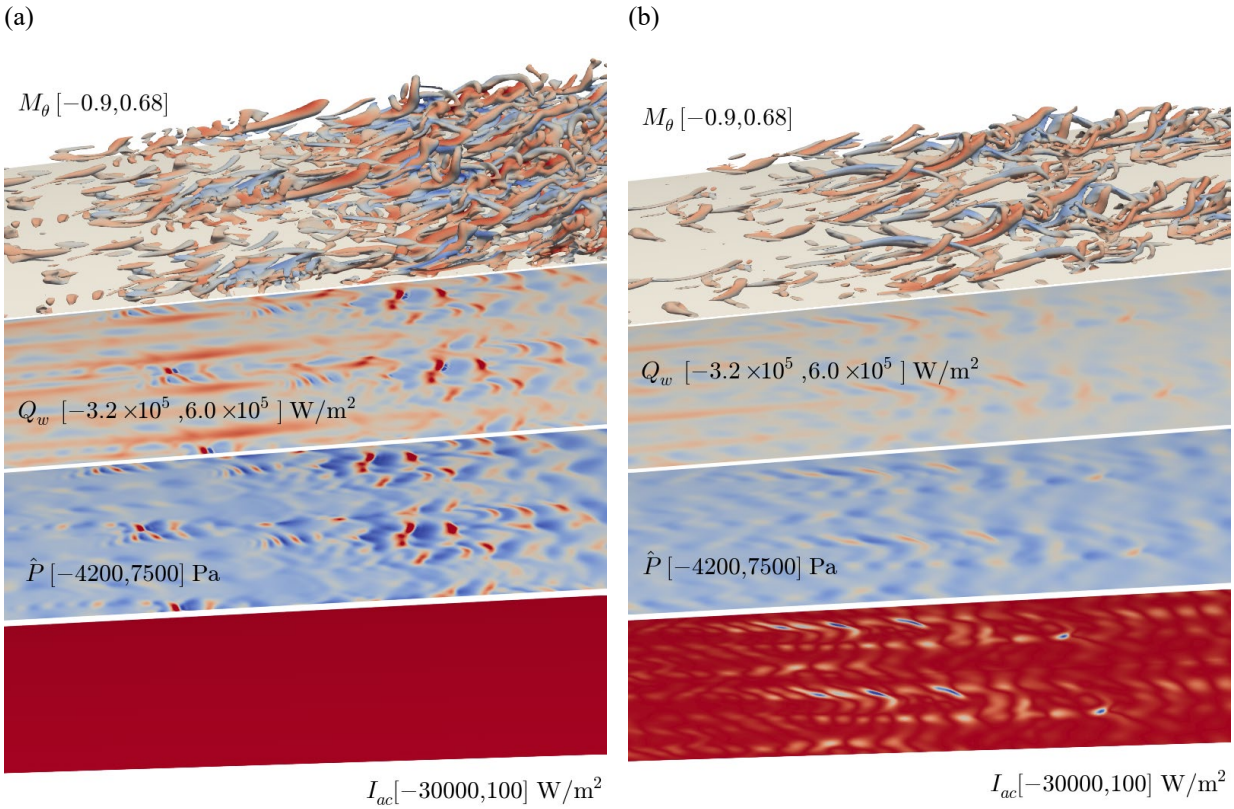

Fig. 19 Comparison between flow quantities in the transitional region between (a) the solid wall and (b) the C/C metasurface. From top to bottom: *Q*-criterion iso-surfaces colored by the Mach number in the azimuthal direction, instantaneous heat flux to the wall, pressure oscillations, and acoustic flux [115].

The other strategy involves directly resolving the detailed BL flow fields that include microstructures. This strategy includes both, a temporal direct numerical simulation (TDNS) and a spatial direct numerical simulation (SDNS). In the TDNS studies (Fig. 20(a)), the initial value problem was solved using the periodic boundary conditions in the *x*-

and z-directions. The forcing terms are included on the right-hand side of the N–S equations to maintain the base flow independent of time. The DNS is initialized with an artificial disturbance of a small amplitude at $t = 0$; the eigenmode is allowed to develop from the initial field. After the transient process, the disturbance exponentially increases with time. The temporal growth rate is calculated as $\alpha_i = d(\ln a)/dt$, where $a(t)$ denotes the disturbance amplitude at a fixed point (x, y, z) [117], and it is consistent with parallel flow approximations typically made in the LST. The TDNS can be considered a tractable DNS, i.e., its computational region only needs one wavelength of the Mack second mode. Although TDNS largely saves computational resources, the first-mode instability will not be captured (even if unstable) because its wavelength is longer than that permitted in the computational domain [72, 118]. In addition, the nonparallel velocity effect, believed to stabilize the Mack second mode and destabilize the first mode, was neglected [119]. The SDNS resolves instability waves that interact with metasurfaces along the streamwise direction; however, this requires abundant computational grids based on the metasurface length.

Brès et al. [72, 118, 120] performed a TDNS of BL flows over a metasurface corrugated with subwavelength microslits. They indicated that metasurface stabilization was directly related to the acoustic absorptive capability of the surface and showed the presence of an unstable mode that appeared in the presence of high porosity with cavities of a moderate aspect ratio that can potentially decrease the overall performance of the metasurface. The stabilization performances of metasurfaces with relatively deep cavities operating in attenuative regimes and of shallow cavities operating in cancellation/reinforcement regimes with alternating regions of local minima and maxima of the acoustic absorption were compared. The numerical simulations confirmed the results of the linear instability theory, which employed impedance boundary conditions. Sandham and Lüdeke [86] conducted TDNS over metasurfaces comprising equally spaced microslits (2D case) and pores with a rectangular cross-section (3D case). They found that the stabilizing effect was stronger than predictions from the LST, with growth rates that are 10%–30% smaller, depending on porosity and pore depth. Fedorov [117] further demonstrated that the discrepancy was caused by the incorrect impedance boundary condition of LST, wherein 2D slits were modeled as cylindrical pores of the equivalent hydraulic radius [86]. For all cases considered in [117], including the 2D microslits and 3D pores of rectangular cross-sections, the LST results agreed well with the numerical solutions if the cross-sectional pore shapes were considered in the calculations of the metasurface impedance. Even in the case of one cavity per disturbance wavelength, the discrepancy between the theoretical and DNS growth rates was less than 1%. Tulio and Sandham [121] investigated turbulence breakdown and reported a reduction in the growth rate of primary and secondary instabilities caused by the presence of regular pores. Further, they found that the oblique first mode wave was destabilized by the metasurfaces, and once the oblique first mode was excited, the flow became turbulent because of the nonlinear interactions without the need for secondary instabilities. Hader et al. [122, 123] applied TDNS to a Mach 6 BL flow and focused on the effect of metasurfaces on the nonlinear regime of transition. A comparison of the amplitude evolution and phase speed locking indicated that the metasurface changed the nature of the nonlinear interaction between the modes and delayed the transition onset (Fig. 21). However, a higher resolution is required to simulate the breakdown regime.

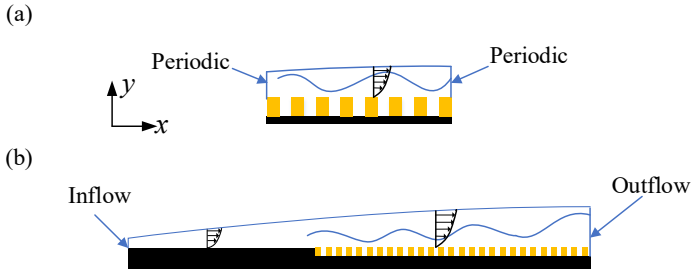

Fig. 20 Schematic of (a) the TDNS and (b) SDNS of the stabilization effect of acoustic metasurfaces

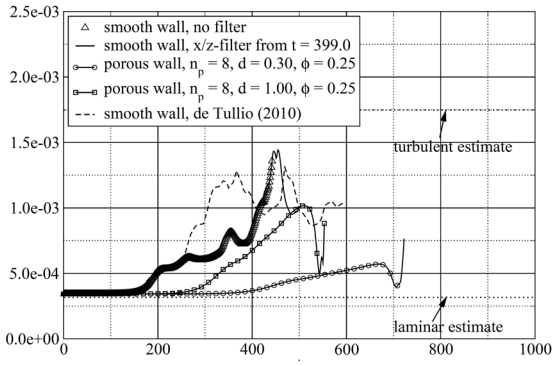

Fig. 21 Comparison of the evolution of averaged skin friction coefficient for smooth wall and metasurface [122].

Zhu et al. [124] used SDNS to investigate the metasurface stabilization effect in a Mach 6 flat-plate BL flow. Their metasurfaces were corrugated with square pores of sequential and interlaced distributions. The DNS results were compared to those of the LST. They found that the metasurface could effectively inhibit the growth rate of the Mack second mode, and the sequence-distributed pores stabilized the BL flow more effectively than the interlace-distributed pores. However, the streamwise computational region was only approximately 2.7δ, where δ denotes the inflow BL thickness. The narrow range neglected the nonparallel and edge effects. Zhao et al. [119] systematically simulated the spatial evolution of disturbances that interacted with the metasurface microstructure, and they emphasized the metasurface effect on the outflow fields, accuracy of the theoretical model, and effect of metasurface locations. In the steady calculation, cavity edges induced alternating expansion and compression waves, and recirculation zones were observed inside cavities. Streamlines were essentially straight near the metasurface (Fig. 22). The BL thickness δ decreased slightly at the metasurface region; however, it quickly recovered to its undisturbed condition on the rigid surface after a short relaxation distance of approximately 5–7δ from the junction. The effect of the metasurface on the mean flow field was sufficiently small to satisfy the "aerodynamically smooth" hypothesis. The impedance boundary could accurately model the metasurface stabilization effect by providing an average treatment of the acoustic characteristics of microcavities when comparing the fluctuating pressure in the metasurface region (Fig. 23). The Mack second mode was destabilized or stabilized when a metasurface was located upstream (Case 1 in Fig. 23) or downstream (Cases 2–3 in Fig. 23) of the synchronization point; this trend was slightly overpredicted by the theoretical mode. Further, they applied SDNS to investigate the BL stabilization effect of the impedance-near-zero metasurface and reflection-controlled one in a Mach 6 flat-plate BL flow [30, 35]. Guo et al. [125] investigated the effect of large cavities in the second mode. The cavity width was approximately 1/3 of the BL thickness δ; however, no new instability mode appeared in the spectrum of the sampling point. In addition, they found that large-sized cavities could help reduce the frictional drag; a reduction of over 40% in the total drag could be achieved when the porosity was 60%.

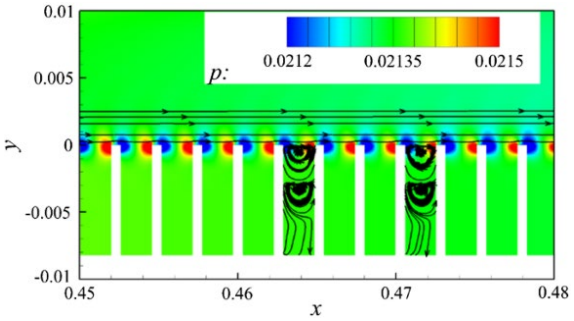

Fig. 22 Local pressure contour around cavities [119].

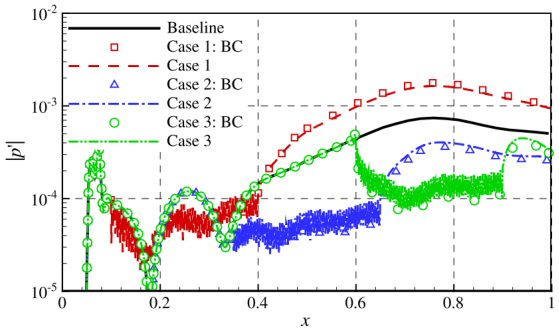

Fig. 23 Comparison of pressure perturbation amplitude distributions predicated by DNS with impedance boundary condition and SDNS along the wall. Baseline is the smooth wall and cases 1–3 denote different metasurface locations [119].

4.3. *Wind tunnel experiments*

Wind tunnel experiments are the most effective approach for evaluating the BL transition control performance of acoustic metasurfaces. The stabilization effect can be checked by measuring the fluctuating flow quantities, and the transition onset point can be determined from the streamwise Stanton number or skin friction distributions. In addition to the general considerations for wind tunnel experiments of hypersonic BL transition, the acoustic metasurface should be carefully designed, manufactured, and installed. Rasheed et al. [62] verified the metasurface transition control concept in the GALCIT T-5 shock tunnel, California Institute of Technology, by testing a 5° half-angle sharp cone. The cone in these tests had one half of its surface solid, and the other half was covered by a porous sheet perforated with equally spaced blind cylindrical holes. Through the laser drilling process, the slightly conical holes were approximately 10–20 holes per disturbance wavelength and with a porosity of 28%. The two halves of the flat sheets (one perforated and one smooth) were rolled to form two longitudinal halves of a cone and then welded by laser fusion along the seams. It took advantage of the mismatch in the thermal expansion coefficients of the stainless-steel cone sheet and aluminum base cone by cooling both parts to 190 K in special freezers. This assembly technique resulted in the cone sheet being stretched tightly over the base cone, which provides blind micropores for the metasurface and eliminates any surface imperfections. Further, it eliminated the need for any mechanical fasteners that would disturb the BL and allow the cone sheet to be nondestructively removable (and thus reusable) by simply reversing the thermal interference fit process. Experiments were performed for ranges of the free-stream total enthalpy, $4.18 \leqslant H_0 \leqslant 13.34 \text{MJ kg}^{-1}$, and the free-stream Mach number, $4.59 \leqslant M_\infty \leqslant 6.4$. For most of the runs, the laminar BL sustained up to the model base on the porous surface half, whereas the transition on the rigid surface was observed halfway along the cone (Fig. 24). Further, they observed that the metasurface could delay the transition under a broad range of inflow Reynolds numbers, whereas the inhibition efficiency decreased as the Reynolds number increased. The LST

comparison was not feasible because the stability characteristics of the BL disturbances were not measured in Ref. [62]; this motivated Fedorov et al. [126] to perform a series of stability experiments (Mach number 5.95) in the open-jet test section of the Institute of Theoretical and Applied Mechanics (ITAM) T-326 hypersonic blowdown wind tunnel. The model was a 7° half-angle sharp with one half of the base part covered by a stainless-steel perforated sheet with equally spaced cylindrical pores of depth h = 450 μm with an approximate porosity of 20%. The perforated sheet was tightly stretched on the cone surface using a custom-built tension mechanism. In addition to the inflow natural disturbances, a 3D actuator was mounted near the cone tip to provide high-frequency artificial wave packets. Using the hot-wire measurement, the metasurface was found to stabilize the second mode and weakly excite the first mode in the natural disturbance case; the LST predictions agreed well with the measured amplitudes of the second-mode disturbances in the artificially excited wave packets.

In the same wind tunnel (ITAM, T-326), experiments were performed to evaluate the stabilization effect of the felt-metal materials [19]. The stainless-steel fibers of diameter d = 30 μm were hard-sintered randomly on a solid stainless-steel sheet and rolled to a porosity of 75%. This resulted in a total thickness of the felt metal sheet of 1 mm with a random pore depth of 0.75 mm. The average pore size was approximately 100 μm, which led to 20 pores per BL disturbance wavelength. After attachment to the basic cone, the felt-metal sheet was ground until the surface irregularity was reduced to 0.05 mm. Like their regular metasurface experiments, the experimental results indicated that the felt-metal strongly stabilized the second mode and marginally destabilized the first mode. Theoretical predictions by LST were in good quantitative agreement with the stability measurements for artificially excited wave packets associated with the second mode. Maslov et al. [127] performed transition experiments on a sharp cone with a felt-metal coating in the Mach 12 hypersonic high-enthalpy wind tunnel AT-303 of ITAM. The porous parameters were the same as those in Ref. [19]. Further, as shown in Fig. 25, the laminarization effect increases with the unit Reynolds number. This trend is unlike that reported in the literature [62], and it may be attributed to the large inflow Mach number under which the Mack second mode is more unstable. The laminar range on the metasurface was doubled that on the solid wall at $Re \approx 2.4\times10^7$/m. Further, they applied the e^N method to predict the transition onset point and found that the location could agree satisfactorily with the experiment when the critical amplification factor $N \approx 5$. Lukashevich et al. [128, 129] systematically investigated the effect of the metasurface length and location on disturbances in a Transit-M hypersonic short-duration wind tunnel under Mach number 5.8. The metasurface was composed of three layers of nylon mesh with a porosity of 44%. They concluded that the effective method to delay transition is to place the acoustic metasurface in a region of second-mode instability, which confirmed the numerical results of Wang and Zhong [107, 108].

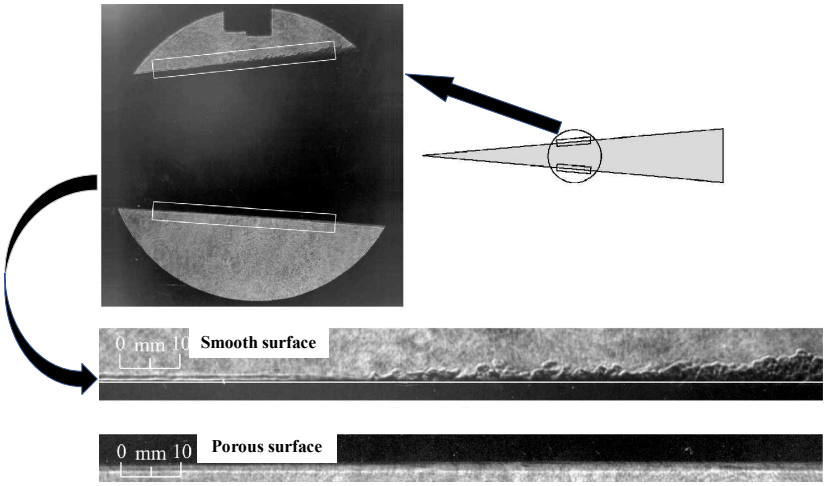

Fig. 24 Resonantly enhanced shadowgraph (inflow total pressure P_0 = 48.2 MPa and total enthalpy H_0 = 9.8 MJ/kg) [62].

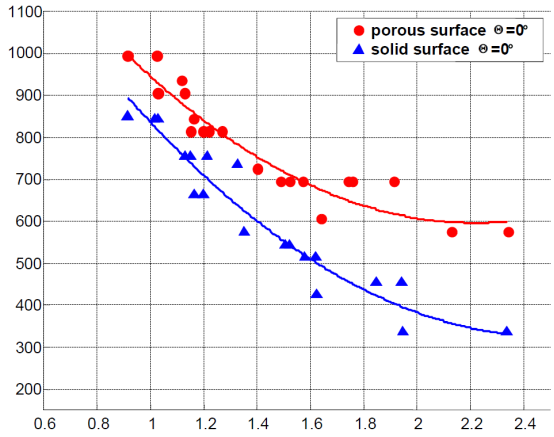

Fig. 25 Points of transition beginning versus the freestream unit Reynolds number [127].

Wagner et al. [64-67] conducted a series of wind tunnel experiments to study the stabilization effect of C/C materials in a high-enthalpy shock tunnel in Göttingen of the German Aerospace Center. The C/C material represents an intermediate state of C/C-SiC that has been successfully used as TPS in hypersonic vehicles [63]. The final C/C-SiC can achieve high porosity without losing the advantages of siliconized ceramics (i.e., oxidation resistance and increased material strength) by optimizing the porous parameters of the C/C ceramic [67]. The free-stream Mach number was 7.5 with the unit Reynolds number varying over a range of Re = 1.5 × 10^6 m^{-1} to 6.4 × 10^6 m^{-1}. The model is a 7° half-angle blunted cone with one-third of its surface covered by C/C. The results indicated that the second-mode instability significantly damped on the C/C surface; the transition onset location was obviously delayed, especially under a high inflow Reynolds number. On the C/C surface, the heat flux scatter around the predicted laminar and turbulent heat flux levels was higher than that of the smooth surface, and this was assumed to be caused by small transducer misalignments on the model surface (Fig. 26).

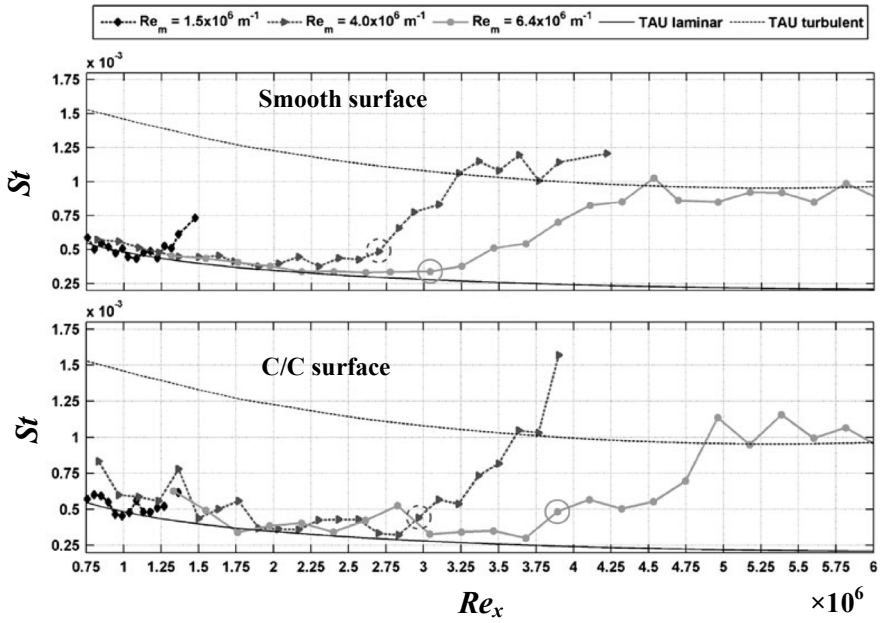

Fig. 26 Normalized heat flux distribution on smooth (upper map) and C/C surface (lower map) for different unit Reynolds numbers (transition Reynolds numbers marked by circles) [64].

Chokani et al. [130] and Bountin et al. [131] used bispectral analysis to study the effect of metasurfaces on the nonlinearity of the second mode. The wind tunnel, test model, and type of metasurface were the same as those in Ref. [126]. The bispectral measurements suggested that the subharmonic and harmonic resonances of the second mode were significantly modified on the metasurface. The harmonic resonance, which is known to be the primary nonlinear mechanism for the breakdown to turbulence in the hypersonic BL on solid surfaces, was completely absent on the metasurface. Further, they observed the subharmonic resonance of the first mode, which was not present on the solid surface. Zhu et al. [68-70] investigated the effect of permeable steel materials on the BL transition in a Mach 6 hypersonic wind tunnel at Peking University. They found that the second mode grew faster in the linear stage and lasted over a longer distance along the flow direction on the permeable wall. However, the bispectral analysis showed that the permeable material disrupts the phase-locked relationship and prevents the growth of fundamental oblique waves, which results in a delayed transition.

5. Prospects

Hypersonic BL transition control is not only a research frontier in fluid mechanics, but also a key technology in the development of hypersonic vehicles, which has both important scientific and engineering significance. Among various transition control technologies, acoustic metasurfaces are emerging, and they can effectively suppress the second mode and delay the BL transition with minimal effects on the mean flow. Further, compared to active technologies, this passive technology is more feasible in practice because of its relatively easy processability and compatibility. Based on the interdisciplinary research generated by structure, acoustics, and fluid mechanics, the following aspects of the acoustic metasurface transition control technology could be further developed.

(1) Mathematical impedance model of acoustic metasurfaces can be used to optimize the metasurface microstructure to obtain specific acoustic characteristics; it can be used as the boundary condition of LST and DNS. However, the current models do not consider flow effects. Influences of recirculation zone inside pores and shear layers at pore edges on the disturbance waves require further study. The roughness effect on the unstable modes,

especially on the first mode, should be considered in the model. Further, when the disturbance wavelength is close to or less than the microstructure width, the impedance model is partially or no longer valid. Under this condition, the influence of the metasurface on the unstable mode is prospected.

(2) There is a lack of sufficient studies on the full hypersonic transition process on acoustic metasurfaces. Interaction mechanisms between nonlinear/turbulent structures and metasurface microstructures should be clarified. The skin friction and heat flux affected by the metasurface in the turbulent region should be evaluated before implementing this technology in applications. Similar to the prospects of impedance models, the range of applications of the TDIBC method should be qualified.

(3) Currently, acoustic metasurfaces are mainly applied to suppress the second mode. However, the dominant mode of transition may change as the flight Mach number and attitude change. The suppression of transition over a wide frequency range by acoustic metasurfaces is an important research direction. Further, most hypersonic vehicles have 3D configurations wherein the crossflow mode may dominate the transition, and thus, the wave control ability of the metasurface needs to be further investigated. Joint active control technologies may be required; for example, the development of micro-blowing/metasurface joint control technology, to achieve a more effective and robust transition control capability.

Acknowledgements

This work was supported by the National Natural Science Foundation of China (Grant No. 11872116, 11991030, and 11991033) and a grant from the Research Grants Council, Hong Kong, under contract Nos. 152041/18E and 152166/21E.

.

References

1. E. Reshotko, Boundary layer stability and transition, Annu. Rev. Fluid Mech. 8 (1976) 311–49.
2. E. Reshotko, Hypersonic stability and transition. In: J. A. Desideri, R. Glowinski, J. Periaux (Eds.), Hypersonic Flows for Reentry Problems, Vol.1, Springer, Berlin, 1991, pp. 18–34.
3. S. P. Schneider, Flight data for boundary layer transition at hypersonic and supersonic speeds. J. Spacecr. Rockets 36 (1999) 8–20.
4. S. P. Schneider, Hypersonic laminar-turbulent transition on circular cones and scramjet forebodies. Prog. Aerosp. Sci. 40 (2004), 1–50.
5. E. Reshotko, Transition issues at hypersonic speeds. AIAA Paper 2006-707.
6. S. P. Schneider. Laminar-turbulent transition on reentry capsules and planetary probes. J. Spacecr. Rockets 43 (2006)1153–73.
7. E. Reshotko, Transition issues for atmospheric entry. J. Spacecr. Rockets 45 (2008) 161–64.
8. A. Fedorov, Transition and Stability of High-Speed Boundary Layers，Annu. Rev. Fluid Mech. 43 (2011) 79–95. https://doi.org/10.1146/annurev-fluid-122109-160750.

9. A. Whitehead, NASP Aerodynamics, in: AIAA First National Aero-Space Plane Conference, Dayton, U.S.A. ,1989, pp. 1-10.

10. A. V. Fedorov, N.D. Malmuth, A. Rasheed, H.G. Hornung, Stabilization of hypersonic boundary layers by porous coatings, AIAA J. 39 (2001) 605–610. https://doi.org/10.2514/3.14776.

11. J. J. Bertin, R.M. Cummings, Critical hypersonic aerothermodynamic phenomena, Annu. Rev. Fluid Mech. 38 (2006) 129–157. https://doi.org/10.1146/annurev.fluid.38.050304.092041.

12. Y. Zhu, D. Gu, W. Zhu, et al, Dilatational-wave-induced aerodynamic cooling in transitional hypersonic boundary layers, J. Fluid Mech. 911 (2021) 1–21. https://doi.org/10.1017/jfm.2020.1044.

13. L.M. Mack, Boundary-layer stability theory, Jet Propulsion Laboratory, California Institute of Technology, Pasadena, California, 1969.

14. E. Reshotko, Boundary layer stability and transition, Annu. Rev. Fluid Mech. 8 (1976) 311–349. https://doi.org/10.1146/annurev.fl.08.010176.001523 .

15. E. Reshotko, Hypersonic stability and transition, in: J.A. Desideri, R. Glowinski, J. Periaux (Eds.), Hypersonic Flows for Reentry Problems, Vol.1, Springer, Berlin, 1991, pp. 18–34.

16. M.V. Morkovin, E. Reshotko, T. Herbert, Transition in open flow systems: a reassessment, Bull. APS. 39 (1994) 1–31.

17. M.R. Malik, T.A. Zang, D.M. Bushnell, Boundary layer transition in hypersonic flows, AIAA Paper 1990-5232.

18. L. M. Mack, Boundary Layer Linear Stability Theory, AGARDRept.709, May 1984.

19. A. V. Fedorov, A.N. Shiplyuk, A.A. Maslov, E. Burov, N.D. Malmuth, Stabilization of a hypersonic boundary layer using an ultrasonically absorptive coating, J. Fluid Mech. 479 (2003) 99–124. https://doi.org/10.1017/S0022112002003440.

20. R.L. Kimmel, Aspects of hypersonic boundary layer transition control, AIAA Paper 772-2003.

21. M.R. Malik, Prediction and control of transition in supersonic and hypersonic boundary layers, AIAA J. 27(11) (1989) 1487–1493. https://doi.org/10.2514/3.10292

22. X. Zhong, X. Wang, Direct Numerical Simulation on the Receptivity, Instability, and Transition of Hypersonic Boundary Layers, Annu. Rev. Fluid Mech. 44 (2012) 527–561. https://doi.org/10.1146/annurev-fluid-120710-101208.

23. A.S.W. Thomas, The control of boundary-layer transition using a wave-superposition principle, J. Fluid Mech. 137(1983) 233–250. https://doi.org/10.1017/s0022112083002384 .

24. I. A. Leyva, J.S Jewell., S. Laurence, J. Shepherd, On the impact of injection schemes on transition in hypersonic boundary layers, AIAA Paper 2009–7204.

25. A.V. Fedorov, V.G. Soudakov, I.A. Leyva, Stability analysis of high-speed boundary-layer flow with gas injection，AIAA Paper 2014–2498.

26. M. Riherd, S. Roy, S. Balachandar, Local stability effects of plasma actuation on a zero pressure gradient boundary layer, Theor. Comput. Fluid Dyn. 28 (2014) 65–87. https://doi.org/10.1007/s00162-013-0302-5..

27. A.V. Fedorov, Prediction and control of laminar-turbulent transition in high-speed boundary-layer flows, Procedia Iutam. 14(2015)3–14. https://doi.org/10.1016/j.piutam.2015.03.017.

28. Development of Ultrasonically Absorptive Aeroshell Materials for Hypersonic Boundary Layer Transition (BLT) Delay, https://www.sbir.gov/node/1532091, 2019. (Accessed 28 November 2018).

29. M. V. Morkovin, Transition at hypersonic speeds, NASA Contract Report No. 178315, June 1987.

30. R. Zhao, T. Liu, C.Y. Wen, J. Zhu, L. Cheng, Impedance-near-zero acoustic metasurface for hypersonic boundary-layer flow stabilization, Phys. Rev. Appl. 11 (2019) 044015. https://doi.org/10.1103/PhysRevApplied.11.044015.

31. H. L. Reed, W. Saric, and D. Arnal, Linear stability theory applied to boundary layers, Ann. Rev. Fluid Mech. 28 (1996), 389–482.

32. I. V. Egorov, A. V. Fedorov, V.G. Soudakov, Direct numerical simulation of disturbances generated by periodic suction-blowing in a hypersonic boundary layer, Theor. Comput. Fluid Dyn. 20 (2006) 41–54. https://doi.org/10.1007/s00162-005-0001-y.

33. R. Zhao, C.Y. Wen, X.D. Tian, T.H. Long, W. Yuan, Numerical simulation of local wall heating and cooling effect on the stability of a hypersonic boundary layer, Int. J. Heat Mass Transf. 121 (2018) 986–998. https://doi.org/10.1016/j.ijheatmasstransfer.2018.01.054.

34. Malmuth N.D., Fedorov A.V., Shalaev V., Cole J., Khokhlov A., Problems in high speed flow prediction relevant to control, AIAA Paper 98–2695.

35. R. Zhao, Y. Dong, X. Zhang, C. Wen, T. Long, W. Yuan, Control of reflected waves with acoustic metasurfaces for hypersonic boundary-layer stabilization. AIAA J. 59(2021)1533. https://doi.org/10.2514/1.J060282.

36. S.O. Stephen, V. Michael, Effects of porous walls on hypersonic boundary layers over a sharp cone, AIAA J. 51 (2013) 1234–1244. https://doi.org/10.2514/1.J052082.

37. P.W. Carpenter, L.J. Porter, Effects of passive porous walls on boundary-layer instability, AIAA J. 39 (2001) 597–604. https://doi.org/10.2514/2.1381.

38. X, Wang, X, Zhong, Phase angle of porous coating admittance and its effect on boundary-layer stabilization, AIAA Paper 2011-3080.

39. X. Tian, R. Zhao, T. Long, C.Y. Wen, Reverse Design of ultrasonic absorptive coating for the stabilization of mack modes, AIAA J. 57 (2019) 2264–2269. https://doi.org/10.2514/1.J058105.

40. R. Zhao, H. Yan, K. Xi, C.Y. Wen, Research on acoustic metasurfaces for the suppression of the first mode, Aeronau. Sci. Tech., 31 (2020) 104-112. https://doi.org/10.19452/j.issn1007-5453.2020.11.013 (in Chinese)

41. N. Bitter, J. Shepherd, Stability of highly cooled hypervelocity boundary layers, J. Fluid Mech., 778 (2015) 586–620.

42. P. V. Chuvakhov, A. V. Fedorov, Spontaneous radiation of sound by instability of a highly cooled hypersonic boundary layer, J. Fluid Mech. **805** (2016) 188–206.

43. C. P. Knisely, X. Zhong, Significant supersonic modes and the wall temperature effect in hypersonic boundary layers, AIAA J. **57** (2018) 1552–1566.

44. C. P. Knisely, X. Zhong, Sound radiation by supersonic unstable modes in hypersonic blunt cone boundary layers. I. Linear stability theory, Phys. Fluids **31** (2019) 024103.

45. C. P. Knisely, X. Zhong, Sound radiation by supersonic unstable modes in hypersonic blunt cone boundary layers. II. Direct numerical simulation, Phys. Fluids **31** (2019) 024104.

46. C. H. Mortensen, Toward an understanding of supersonic modes in boundary-layer transition for hypersonic flow over blunt cones, J. Fluid Mech. 846 (2018) 789–814.

47. T. Long, Y. Dong, R. Zhao, C. Wen, Mechanism of stabilization of porous coatings on unstable supersonic mode in hypersonic boundary layers, Phys. Fluids. 33 (2021) 054105. https://doi.org/10.1063/5.0048313.

48. P. E. Doak, Momentum potential theory of energy flux carried by momentum fluctuations, J. sound and Vib. 131 (1989) 67–90.

49. P. E. Doak, Fluctuating total enthalpy as the basic generalized acoustic field, Theor. Comput. Fluid Dyn. **10** (1998) 115–133.

50. S. Unnikrishnan, D. V. Gaitonde, Interactions between vortical, acoustic and thermal components during hypersonic transition, J. Fluid Mech. 868 (2019) 611–647. https://doi.org/10.1017/jfm.2019.176..

51. S. Unnikrishnan, D. V. Gaitonde, Instability characteristics of cooled hypersonic boundary layers, AIAA Paper 2020-0588 .

52. S. Unnikrishnan, D. V. Gaitonde, Instabilities and transition in cooled wall hypersonic boundary layers, J. Fluid Mech. 915 (2021) 1–38. https://doi.org/10.1017/jfm.2021.84.

53. Y. Li, B. Liang, Z. M. Gu, X. Y. Zou, J. C. Cheng, Reflected wavefront manipulation based on ultrathin planar acoustic metasurfaces, Sci. Rep. 3(2013)2546. https://doi.org/10.1038/srep02546.

54. J. Zhao, B. Li, Z. Chen, C.W. Qiu, Manipulating acoustic wavefront by inhomogeneous impedance and steerable extraordinary reflection, Sci. Rep. 3(2013)2537. https://doi.org/10.1038/srep02537.

55. Y. Xie, W. Wang, H. Chen, A. Konneker, B. I. Popa, S. A. Cummer, Wavefront modulation and subwavelength diffractive acoustics with an acoustic metasurface, Nat. Commun. 5(2014) 6553.https://doi.org/10.1038/ncomms6553 ..

56. K. Tang, C. Qiu, M. Ke, J. Lu, Y. Ye, Z. Liu, Anomalous refraction of airborne sound through ultrathin metasurfaces, Sci. Rep. 4(2014)06517.https://doi.org/10.1038/srep06517.

57. Y. Li, X. Jiang, R. Q. Li, B. Liang, X. Y. Zou, L. L. Yin, J. C. Cheng, Experimental realization of full control of reflected waves with subwavelength acoustic metasurfaces, Phys. Rev. Appl. 2(2014)064002. https://doi.org/10.1103/physrevapplied.2.064002 .

58. Y. Li, X. Jiang, B. Liang, J. C. Cheng, L. K. Zhang, Metascreen-Based Acoustic Passive Phased Array, Phys. Rev. Appl. 4(2015)024003. https://doi.org/10.1103/physrevapplied.4.024003 ..

59. G. Ma, M. Yang, S. Xiao, Z. Yang, P. Sheng, Acoustic metasurface with hybrid resonances, Nat. Mater. 13 (2014)873-878. https://doi.org/10.1038/nmat3994.

60. Y. Cheng, C. Zhou, B. G. Yuan, D. J. Wu, Q. Wei, X. J. Liu, Ultra-sparse metasurface for high reflection of low-frequency sound based on artificial Mie resonances, Nat. Mater. 14(2015)1013-1019.https://doi.org/10.1038/nmat4393.

61. Y. Li and B. M. Assouar, Acoustic metasurface-based perfect absorber with deep subwavelength thickness, Appl. Phys. Lett. 108(2016)063502.https://doi.org/10.1063/1.4941338.

62. A. Rasheed, H.G. Hornung, A. V. Fedorov, N.D. Malmuth, Experiments on passive hypervelocity boundary-layer control using an ultrasonically absorptive surface, AIAA J. 40 (2002) 481–489. https://doi.org/10.2514/2.1671.

63. J. Turner, M. Horschgen, W. Jung, A. Stamminger, P. Turner, SHEFEX - Hypersonic Re-entry Fllight Experiment - Vehicle and Subsystem Design, Flight Performance and Prospects, AIAA Paper 2006-8115.

64. A. Wagner, M. Kuhn, J. Martinez Schramm, K. Hannemann, Experiments on passive hypersonic boundary layer control using ultrasonically absorptive carbon-carbon material with random microstructure, Exp. Fluids. 54 (2013). https://doi.org/10.1007/s00348-013-1606-3..

65. A. Wagner, Passive hypersonic boundary layer transition control using ultrasonically absorptive carbon–carbon ceramic with random microstructure, Ph.D. thesis, Belgium: Katholieke Universiteit Leuven, 2014.

66. A. Wagner, M. Kuhn, J. Martinez Schramm, K. Hannemann, Experiments on passive hypersonic boundary layer control using ultrasonically absorptive carbon-carbon material with random microstructure, Exp. Fluids. 54 (2013). https://doi.org/10.1007/s00348-013-1606-3..

67. A. Wagner, V. Wartemann, K. Hannemann, M. Kuhn, C. Dittert, The potential of ultrasonically absorptive tps materials for hypersonic vehicles, AIAA Paper 2015-3576.

68. W. Zhu, M. Shi, Y. Zhu, C. Lee, Experimental study of hypersonic boundary layer transition on a permeable wall of a flared cone, Phys. Fluids. 32 (2020). https://doi.org/10.1063/1.5139546.

69. W. Zhu, M. Shi, C. Lee, Experimental and theoretical study of the hypersonic boundary layer transition on the permeable wall of a flared cone, AIAA Paper 2020-2964.

70. W. Zhu, X. Chen, Y. Zhu, C. Lee, Nonlinear interactions in the hypersonic boundary layer on the permeable wall, Phys. Fluids. 32 (2020)104110. https://doi.org/10.1063/5.0028698.

71. G.A. Brès, T. Colonius, A. V. Fedorov, Acoustic properties of porous coatings for hypersonic boundary-layer control, AIAA J. 48 (2010) 267–274. https://doi.org/10.2514/1.40811.

72. G.A. Brès, M. Inkman, T. Colonius, A. V Fedorov, Second-mode attenuation and cancellation by porous coatings in a high-speed boundary layer, J. Fluid Mech. 726 (2013) 312–337. https://doi.org/10.1017/jfm.2013.206.

73. N. Yu, P. Genevet，M. A. Kats, F. Aieta, J.-P. Tetienne, F. Capasso, Z. Gaburro, Light propagation with phase discontinuities: generalized laws of reflection and refraction, Science. 334(2011) 333–337. https://doi.org/10.1126/science.1210713.

74. Asadchy V. S., Albooyeh M., Tcvetkova S. N., A. Diacuteaz-Rubio, Y. Ra'di, S. A. Tretyakov, Perfect control of reflection and refraction using spatially dispersive metasurfaces, Phys. Rev. B. 94(2016) 075142. https://doi.org/10.1103/PhysRevB.94.075142 ..

75. S. A. Gaponov, Influence of porous layer on boundary-layer stability, Izevestia SO AN SSSR, Seria Technicheskich Nauk, Vyp. 1, (1971), 21–23 (in Russian).

76. S. A. Gaponov, Influence of gas compressibility on stability of boundary layer on porous surface at subsonic speeds, Zhurnal Prikladnoi Mechaniki i Technicheskoi Fiziki. 1 (1975), 121–125 (in Russian).

77. S. A. Gaponov, Stability of supersonic boundary layer on porous wall with heat conductivity, Izvestia AN SSSR, Mechanika Zhidkosti I Gaza, 1, (1977), 41–46 (in Russian).

78. M. R. Stinson, Y. Champoux, Propagation of sound and the assignment of shape factors in model porous materials having simple pore geometries, J. Acoust. Soc. Am. 91(1992) 685-695. https://doi.org/10.1121/1.402530

79. F.B. Daniels, On the propagation of sound waves in a cylindrical conduit, J. Acoustic. Soc. Am. 22(1950) 563-564. https://doi.rog/10.1121/1.1906650.

80. A. H. Benade, On the propagation of sound waves in a cylindrical conduit, J. Acoustic. Soc. Am. 44(1968) 616-623. https://doi.org/10.1121/1.1906650

81. D. L. Johnson, J. Koplik, R. Dashen, Theory of dynamic permeability and tortuosity in fluid saturated porous media, J. Fluid Mech. 176(1987) 379–402. https://doi.org/10.1017/s0022112087000727

82. A. A. Maslov, Experimental and theoretical studies of hypersonic laminar flow control using ultrasonically absorptive coatings (UAC), in: International Science and Technology Center Rept., Moscow, May. 2003, pp. 2172–2001.

83. V.F. Kozlov, A. V Fedorov, N.D. Malmuth, Acoustic properties of rarefied gases inside pores of simple geometries, J. Acoust. Soc. Am. 117 (2005) 3402–3412. https://doi.org/10.1121/1.1893428.

84. R. Zhao, T. Liu, C.Y. Wen, J. Zhu, L. Cheng, Theoretical modeling and optimization of porous coating for hypersonic laminar flow control, AIAA J. 56 (2018) 2942–2946. https://doi.org/10.2514/1.J057272.

85. R. Zhao, X.X. Zhang, C.Y. Wen, Theoretical modeling of porous coatings with simple microstructures for hypersonic boundary-layer stabilization, AIAA J. 58 (2020) 981–986. https://doi.org/10.2514/1.J058403.

86. N.D. Sandham, H. Lüdeke, Numerical study of Mach 6 boundary-layer stabilization by means of a porous surface, AIAA J. 47 (2009) 2243–2252. https://doi.org/10.2514/1.43388.

87. A. Fedorov, A. Shiplyuk, A. Maslov, E. Burov, N. Malmuth, Stabilization of a hypersonic boundary layer using an ultrasonically absorptive coating – CORRIGENDUM, J. Fluid Mech. 769 (2015) 725–728. https://doi.org/10.1017/jfm.2015.155.

88. R.C. Tritarelli, S.K. Lele, A. V. Fedorov, Stabilization of a hypersonic boundary layer using a felt-metal porous coating, J. Fluid Mech. 769 (2015) 729–739. https://doi.org/10.1017/jfm.2015.156.

89. D. Patel, P. Gupta, C. Scalo, T. Rothermel, M. Kuhn, Towards impedance characterization of carbon-carbon ultrasonically absorptive cavities via the inverse Helmholtz problem, AIAA Paper 2019-2151.

90. D. Patel, P. Gupta, C. Scalo, Surface impedance determination via numerical resolution of the inverse Helmholtz problem, AIAA Paper 2017-3695.

91. A. Wagner, J. Martinez Schramm, C. Dittert, V. Sousa, D.I. Patel, C. Scalo, Experimental and numerical acoustic characterization of ultrasonically absorptive porous materials, AIAA Paper 2018-2948.

92. M. A. Delany, E.N. Bazley, Acoustic properties of fibrous absorbent materials, Appl. Acoust. 3(1970) 105–116. https://doi.org/10.1016/0003-682X(70)90031-9.

93. C. Zwikker, C. W. Kosten, Sound Absorbing Materials, Elsevier, New York, 1949.

94. J.-F. Allard, Y. Champoux, Empirical equations for sound propagation in rigid frame porous materials, J. Acoust. Soc. Am. 91(1992)3346–3353. https://doi.org/10.1121/1.402824.

95. V.C.B.B. Sousa, D. Patel, J.-B.B. Chapelier, V. Wartemann, A. Wagner, C. Scalo, Numerical investigation of second-mode attenuation over Carbon/Carbon porous surfaces, J. Spacecr. Rockets. 56 (2019) 319–332. https://doi.org/10.2514/1.A34294.

96. M. Möser, Engineering Acoustics: an Introduction to Noise Control, 2nd ed. Springer, 2009.

97. L M. Mack, Boundary-layer stability theory, Jet Propulsion Laboratory, California Institute of Technology, Pasadena, California, 1969.

98. V. Wartemann, H. Lüdeke, N.D. Sandham, Stability analysis of hypersonic boundary layer flow over microporous surfaces, AIAA Paper 2009-7202.

99. G. Bres, T. Colonius, A. Fedorov, Interaction of acoustic disturbances with micro-cavities for ultrasonic absorptive coatings, AIAA Paper 2008-3903.

100. R.C. Tritarelli, S.K. Lele, A. V. Fedorov, Stabilization of a hypersonic boundary layer using a felt-metal porous coating, J. Fluid Mech. 769 (2015) 729–739. https://doi.org/10.1017/jfm.2015.156.

101. V. Wartemann, A. Wagner, T. Eggers, K. Hannemann, Passive hypersonic boundary layer control by means of ultrasonically absorptive carbon-carbon ceramics: Investigations of different boundary conditions, AIAA Paper 2015-3577.

102. S. V Lukashevich, A.A. Maslov, A.N. Shiplyuk, A. V. Fedorov, V.G. Soudakov, Stabilization of high-speed boundary layer using porous coatings of various thicknesses, AIAA J. 50 (2012) 1897–1904. https://doi.org/10.2514/1.J051377.

103. J. Xu, J. Liu, S. Mughal, P. Yu, J. Bai, Secondary instability of Mack mode disturbances in hypersonic boundary layers over micro-porous surface, Phys. Fluids. 32 (2020) 044105. https://doi.org/10.1063/5.0001914.

104. T. Herbert, Secondary instability of boundary layers, Annu. Rev. Fluid Mech. 20(1988)487–526. https://doi.org/10.1146/annurev.fl.20.010188.002415.

105. I. V Egorov, A. V Fedorov, A. V Novikov, V. G. Soudakov, Direct numerical simulation of supersonic boundary-layer stabilization by porous coatings, AIAA Paper 2007-948.

106. X. Wang, X. Zhong, Role of the synchronization point on boundary layer stabilization using porous coating, AIAA Paper 2008-4382.

107. X. Wang, X. Zhong, Effect of porous coating on boundary-layer instability, AIAA Paper 2010-1243.

108. X. Wang, X. Zhong, The stabilization of a hypersonic boundary layer using local sections of porous coating, Phys. Fluids. 24 (2012) 034105. https://doi.org/10.1063/1.3694808..

109. X. Wang, X. Zhong, Numerical simulations on mode S growth over feltmetal and regular porous coatings of a Mach 5. 92 flow, AIAA Paper 2011-375.

110. X.Y. Li, X.D. Li, C.K.W. Tam, Improved multipole broadband time-domain impedance boundary condition, AIAA J. 50 (2012) 980–984. https://doi.org/10.2514/1.J051361.

111. V. Sousa, D. Patel, J.-B.B. Chapelier, V. Wartemann, A. Wagner, C. Scalo, Numerical Investigation of Second-Mode Attenuation over Carbon/Carbon Porous Surfaces, J. Spacecr. Rockets. 56 (2019) 319–332. https://doi.org/10.2514/1.A34294.

112. K.Y. Fung, H. Ju, Time-domain impedance boundary conditions for computational acoustics and aeroacoustics, Int. J. Comut. Fluid Dyn. 18 (2004) 503–511. https://doi.org/10.1080/10618560410001673515.

113. T. J. Poinsot, S. K. Lele, Boundary conditions for direct simulations of compressible viscous flows, J. Comput. Phys. 101(1992) 104–129. https://doi.org/10.1016/0021-9991(92)90046-2.

114. C. Scalo, J. Bodart, S.K. Lele, Compressible turbulent channel flow with impedance boundary conditions, Phys. Fluids. 27 (2015) 035107. https://doi.org/10.1063/1.4914099..

115. V. Sousa, V. Wartemann, A. Wagner, Carlo Scalo. Towards direct numerical simulation of hypersonic transition delay via distributed wall porosity, AIAA Paper 2019-2151.

116. Y. Chen, C. Scalo, Trapped waves in supersonic and hypersonic turbulent channel flow over porous walls, J. Fluid Mech. 920 (2021) 1–37. https://doi.org/10.1017/jfm.2021.428.

117. A. V. Fedorov, Temporal stability of hypersonic boundary layer on porous wall: comparison of theory with DNS, AIAA Paper 2010-1242.

118. G.A. Bres, T. Colonius, A. V. Fedorov, Stability of temporally evolving supersonic boundary layers over micro-cavities for ultrasonic absorptive coatings, AIAA Paper 2008-4337.

119. R. Zhao, C.Y. Wen, T.H. Long, X.D. Tian, L. Zhou, Y. Wu, Spatial direct numerical simulation of the hypersonic boundary-layer stabilization using porous coatings, AIAA J. 57 (2019) 5061–5065. https://doi.org/10.2514/1.J058467.

120. G.A. Bres, M. Inkman, T. Colonius, A. V. Fedorov, Alternate Designs of Ultrasonic Absorptive Coatings for Hypersonic Boundary Layer Control, AIAA Paper 2009-4217..

121. N. De Tullio, N.D. Sandham, Direct numerical simulation of breakdown to turbulence in a Mach 6 boundary layer over a porous surface, Phys. Fluids. 22 (2010). https://doi.org/10.1063/1.3481147.

122. C. Hader, C. Brehm, H.F. Fasel, Numerical Investigation of transition delay in a Mach 6 Boundary Layer using porous walls, AIAA Paper 2013-2740.

123. C. Hader, C. Brehm, H.F. Fasel, Numerical investigation of transition delay for various controlled breakdown scenarios in a Mach 6 Boundary Layer using porous walls, AIAA Paper 2014-2500.

124. D. H. Zhu, Z. Y. Liu, X. J. Yuan. Mechanism of transition delay by porous surface in hypersonic boundary layers, Chin. J. Comput. Phys. 33 (2016) 163-169. (in Chinese). https://doi.org/10.3969/j.issn.1001-246X.2016.02.005

125. Q. L. Guo, G. H. Tu, J. Q. Chen, X. X.Yuan, B. B. Wan. Control of hypersonic boundary layer instability by transverse rectangular micro-cavities. J. Aerosp. Power, 35, (2020) 135-143. (in Chinese). https://doi.org/10.13224/j.cnki.jasp.2020.01.016.

126. A. V. Fedorov, V.F. Kozlov, A.N. Shiplyuk, A. a. Maslov, N.D. Malmuth, Stability of hypersonic boundary layer on porous wall with regular microstructure, AIAA J. 44 (2006) 1866–1871. https://doi.org/10.2514/1.21013.

127. A. Maslov, A. Shiplyuk, A. Sidorenko, P. Polivanov, A. Fedorov, V. Kozlov, N. Malmuth, Hypersonic laminar flow control using a porous coating of random microstructure, AIAA Paper 2006-1112.

128. S. V Lukashevich, S.O. Morozov, A.N. Shiplyuk, Experimental study of the effect of a passive porous coating on disturbances in a hypersonic boundary layer. 1. Effect of the porous coating length, J. Appl. Mech. Tech. Phys. 54 (2013) 572–577. https://doi.org/10.1134/S002189441304007X.

129. S. V Lukashevich, S.O. Morozov, A.N. Shiplyuk, Experimental study of the effect of a passive porous coating on disturbances in a hypersonic boundary layer 2. Effect of the porous coating location, J. Appl. Mech. Tech. Phys. 57 (2016) 873–878. https://doi.org/10.1134/S002189441605014X.

130. N. Chokani, D.A. Bountin, A.N. Shiplyuk, A.A. Maslov, Nonlinear aspects of hypersonic boundary-layer stability on a porous surface, AIAA J. 43 (2005) 149–155. https://doi.org/10.2514/1.9547.

131. D.A. Buntin, A.A. Maslov, T.A. Chimytov, A.N. Shiplyuk, Bispectral analysis of nonlinear processes in the hypersonic boundary layer on a porous cone surface, Fluid Dyn. 45 (2010) 415–421. https://doi.org/10.1134/S0015462810030087.